Cross-scale observations of the 2015 St. Patrick's day storm: THEMIS, Van Allen Probes, and TWINS

J. Goldstein[1,2] (ID), V. Angelopoulos[3], S. De Pascuale[4] (ID), H. O. Funsten[5] (ID), W. S. Kurth[4] (ID), K. LLera[1,2] (ID), D. J. McComas[6] (ID), J. D. Perez[7] (ID), G. D. Reeves[5] (ID), H. E. Spence[8] (ID), S. A. Thaller[9] (ID), P. W. Valek[1,2] (ID), and J. R. Wygant[9] (ID)

[1]Space Science and Engineering Division, Southwest Research Institute, San Antonio, Texas, USA, [2]Department of Physics and Astronomy, University of Texas at San Antonio, San Antonio, Texas, USA, [3]Institute of Geophysics and Planetary Physics, University of California, Los Angeles, California, USA, [4]Department of Physics and Astronomy, University of Iowa, Iowa City, Iowa, USA, [5]Los Alamos National Laboratory, Los Alamos, New Mexico, USA, [6]Department of Astrophysical Science, Princeton University, Princeton, New Jersey, USA, [7]Physics Department, Auburn University, Auburn, Alabama, USA, [8]Institute for the Study of Earth, Oceans, and Space, University of New Hampshire, Durham, New Hampshire, USA, [9]Department of Physics and Astronomy, University of Minnesota, Twin Cities, Minneapolis, Minnesota, USA

Abstract We present cross-scale magnetospheric observations of the 17 March 2015 (St. Patrick's Day) storm, by Time History of Events and Macroscale Interactions during Substorms (THEMIS), Van Allen Probes (Radiation Belt Storm Probes), and Two Wide-angle Imaging Neutral-atom Spectrometers (TWINS), plus upstream ACE/Wind solar wind data. THEMIS crossed the bow shock or magnetopause 22 times and observed the magnetospheric compression that initiated the storm. Empirical models reproduce these boundary locations within 0.7 R_E. Van Allen Probes crossed the plasmapause 13 times; test particle simulations reproduce these encounters within 0.5 R_E. Before the storm, Van Allen Probes measured quiet double-nose proton spectra in the region of corotating cold plasma. About 15 min after a 0605 UT dayside southward turning, Van Allen Probes captured the onset of inner magnetospheric convection, as a density decrease at the moving corotation-convection boundary (CCB) and a steep increase in ring current (RC) proton flux. During the first several hours of the storm, Van Allen Probes measured highly dynamic ion signatures (numerous injections and multiple spectral peaks). Sustained convection after ∼1200 UT initiated a major buildup of the midnight-sector ring current (measured by RBSP A), with much weaker duskside fluxes (measured by RBSP B, THEMIS a and THEMIS d). A close conjunction of THEMIS d, RBSP A, and TWINS 1 at 1631 UT shows good three-way agreement in the shapes of two-peak spectra from the center of the partial RC. A midstorm injection, observed by Van Allen Probes and TWINS at 1740 UT, brought in fresh ions with lower average energies (leading to globally less energetic spectra in precipitating ions) but increased the total pressure. The cross-scale measurements of 17 March 2015 contain significant spatial, spectral, and temporal structure.

1. Introduction

Geomagnetic storms are driven by both external solar wind forcing and internal feedback involving coupling among different magnetospheric plasmas. Consequently, geospace plasmas and fields possess structure on diverse spatial scales, dynamically linked to each other in various time-dependent ways, perhaps especially for large storms. The contemporary availability of multiple, simultaneously operating magnetospheric space missions presents an opportunity to study the storm time response of near-Earth plasmas on scales from local to global.

The Time History of Events and Macroscale Interactions during Substorms (THEMIS) mission is a three-satellite constellation (THEMIS a, THEMIS d, and THEMIS e) that samples the magnetosphere in highly elliptical orbits with near-equatorial inclinations [*Angelopoulos*, 2008; *Angelopoulos and et al.*, 2008]. On board each of THEMIS a, THEMIS d, and THEMIS e are electrostatic analyzers (ESAs) that measure magnetospheric ions between 6 eV and 25 keV [*McFadden et al.*, 2008]. The high (∼12 R_E) apogee permits the study of the magnetotail (on the nightside) and the bow shock/magnetopause boundary (on the dayside).

The Van Allen Probes mission, formerly known as the Radiation Belt Storm Probes (RBSP), consists of two identical spacecraft (RBSP A and RBSP B) in low-inclination, highly elliptical (1.1 R_E by 5.8 R_E) orbits that sample

the inner magnetosphere and radiation belts [*Mauk et al.*, 2013]. The Helium, Oxygen, Proton, and Electron (HOPE) mass spectrometer obtains species-separated ion fluxes in the energy range 1 eV (above spacecraft potential) to 50 keV [*Funsten et al.*, 2013]. The Electric and Magnetic Field Instrument Suite and Integrated Science (EMFISIS) suite measures plasma waves from which electron number densities may be derived [*Kletzing et al.*, 2013]. The Electric Field and Waves (EFW) suite measures quasi-static, low-frequency fields associated with particle acceleration and transport [*Wygant et al.*, 2013].

Two Wide-angle Imaging Neutral-atom Spectrometers (TWINS) is a stereo magnetospheric imaging mission comprising two spacecraft (TWINS 1 and TWINS 2) in widely separated (in local time) Molniya orbits [*McComas et al.*, 2009]. On board each TWINS spacecraft is a wide-field (140°) camera that measures energetic neutral atoms (ENAs) to perform remote sensing of the terrestrial ring current. ENA images are routinely deconvolved via numerical inversion, to yield global maps of magnetospheric ions between 1 and 100 keV [*Goldstein and McComas*, 2013].

Together, these three multiprobe missions make up an observatory for the study of cross-scale magnetospheric physics. The in situ measurements (THEMIS and Van Allen Probes) give a detailed view of small-scale structures and processes all along individual orbits, though each point is sampled at a different time. Global images (TWINS) provide macroscale contextual and quantitative information, simultaneously over a broad region of space. These cross-scale observations, from multiple missions, are necessary to understand the interconnectivity of different regions and populations in geospace [*Goldstein and McComas*, 2013; *NASA Heliophysics Roadmap*, 2014]. In this study we use multiprobe measurements by THEMIS, Van Allen Probes, and TWINS to study dynamic linkages among different regions of the Earth's magnetosphere, from the dayside boundary to the inner magnetosphere. The combined use of all three of these mission data sets yields a more comprehensive picture of cross-scale dynamics than any one mission — or even two missions — can provide. This study thus builds upon previous results that used TWINS images together with data from either THEMIS or Van Allen Probes [*Fok et al.*, 2010; *Grimes et al.*, 2013; *Keesee et al.*, 2014a; *Perez et al.*, 2012, 2015; *Fok et al.*, 2014; *Valek et al.*, 2015] and complements previous work correlating the dynamics of the ring current with that of the dayside boundary (observed by Interstellar Boundary Explorer (IBEX)) [*McComas et al.*, 2012].

In this paper we present cross-scale magnetospheric observations of the 17 March 2015 (St. Patrick's Day) storm, obtained by THEMIS, the Van Allen Probes, and TWINS. In section 2 we describe the storm event and the mission constellation. In section 3 we present THEMIS observations of the magnetospheric compression that initiated the storm and compare them to model predictions. Section 4 interprets plasmapause encounters by the Van Allen Probes, using a simulation for global context. In section 5, we study ring current dynamics using both in situ data (Van Allen Probes and THEMIS) and TWINS images. We discuss and summarize our results in sections 6 and 7. The cross-scale measurements (interpreted with the help of models) contain a great deal of spatial, spectral, and temporal structure, suggesting that storm time plasma transport comprises a large number of individual, bursty flows, and ion structures. During the main phase, all three missions measured a two-peak ion spectrum in the center of the partial ring current. We find that multimission measurements, combined with simple models, can provide a more complete picture of the storm than any one source of information.

2. 2015 St. Patrick's Day Event

In this section we describe the storm event, and the mission constellation used to observe it.

2.1. Solar Wind and Geomagnetic Conditions

Figure 1 summarizes the solar wind and geomagnetic conditions on 17 March 2015. The B_Z component of the interplanetary magnetic field (Figure 1a) and solar wind pressure P_{SW} (Figure 1b) were recorded upstream by the Advanced Composition Explorer (ACE) [*Stone et al.*, 1998] before 0700 UT and after 1700 UT and by Wind [*Ogilvie et al.*, 1995; *Lepping et al.*, 1995] during 0900–1500 UT. These data were propagated to the Earth by the (Space Physics Data Facility) SPDF/OMNI data service. During 0700–0900 UT and 1500–1700 UT there were gaps in OMNI coverage. These gaps resulted from a lack of plasma data from both ACE and Wind. However, ACE magnetic data are available for these gap intervals. The ACE B_Z data were propagated to the dayside magnetopause ($\Delta T = X/V_{SW}$) and are given by the gray traces plotted in the OMNI data gaps. Using the interplanetary magnetic field (IMF) and solar wind pressure as inputs, the magnetopause standoff distance (Figure 1c) was computed using the model of *Shue et al.* [1997]. Figure 1d shows the standard 1 h *Dst* index.
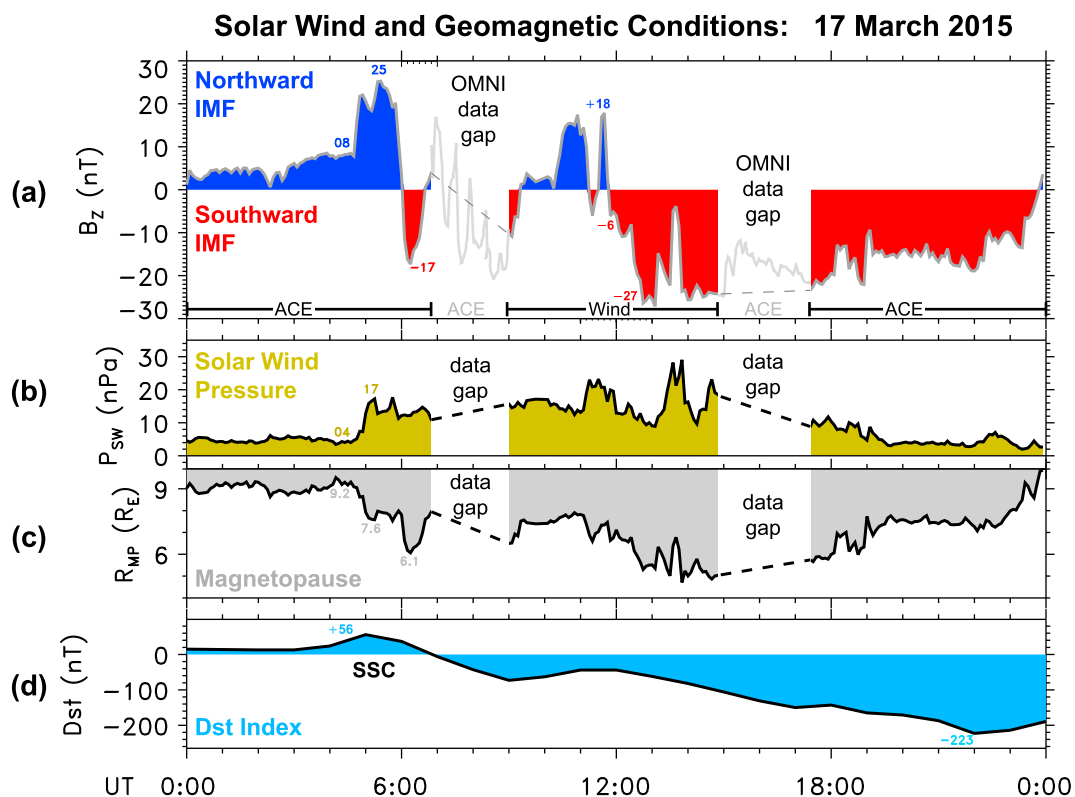
Figure 1. Solar wind and geomagnetic conditions during 2015 St. Patrick's Day storm. OMNI solar wind data were measured by ACE and Wind. (a) B_Z IMF component. (b) Solar wind pressure P_{SW}. (c) *Shue et al.* [1997] magnetopause standoff, R_{MP}. (d) *Dst* index (Kyoto).

The day began with >4 nT northward IMF and > 4 nPa solar wind pressure. At ∼0500 UT, the IMF rotated more strongly northward (from 8 nT to 25 nT), and the solar wind pressure ramped up from 4 nPa to 17 nPa, compressing the magnetosphere. The model subsolar magnetopause moved from 9.2 R_E to 7.6 R_E. This magnetopause compression was accompanied by a storm sudden commencement (SSC) signature; i.e., *Dst* rose to 56 nT. At about 0600 UT the IMF turned to a southward value of −17 nT, eroding the already-compressed magnetopause further, to 6.1 R_E and driving *Dst* negative, i.e., initiating the main phase of the storm. Following ∼2 h of mostly southward IMF (as given by the ACE data during the 0700–0900 UT OMNI data gap) and a ∼2 h northward interval, at about 1200 UT the IMF rotated to strongly southward (−10 to −27 nT) orientation and remained so for most of the rest of the day. As a result, the magnetopause standoff distance was pushed inside geosynchronous orbit for several hours (until ∼1800 UT), and *Dst* reached a minimum value of −223 nT at 2200 UT.

2.2. Mission Constellation

Figure 2 shows the *X-Y* and *X-Z* planes, in solar magnetic (SM) coordinates [*Kivelson and Russell*, 1995], with the Sun to the right. The gray circle in Figure 2a is geosynchronous orbit (6.6 R_E). The gray dipole field lines in Figure 2b at L = 6.6 are plotted merely as a visual guide; the magnetosphere was strongly nondipolar for this storm, given the significant compression by the solar wind, already noted earlier. The yellow regions in Figure 2 indicate the magnetosheath, bounded by the magnetopause (solid green curve) and the bow shock (dashed green curve). Both the magnetopause and the bow shock curves were computed from models, with the IMF and solar wind pressure of Figure 1 as inputs. The magnetopause model is that of *Shue et al.* [1997], which was formulated based on data from ISEE 1 and ISEE 2, AMPTE/IRM, and IMP 8. The bow shock model is that of *Jelínek et al.* [2012], based on THEMIS data. These two boundary models are used throughout this study. At the 1805 UT snapshot shown in Figure 2, the subsolar magnetopause was compressed inside geosynchronous orbit.

Depicted in Figure 2 are the orbits of THEMIS, Van Allen Probes, and TWINS at 1805 UT on 17 March 2015, several hours into the main phase of the storm.
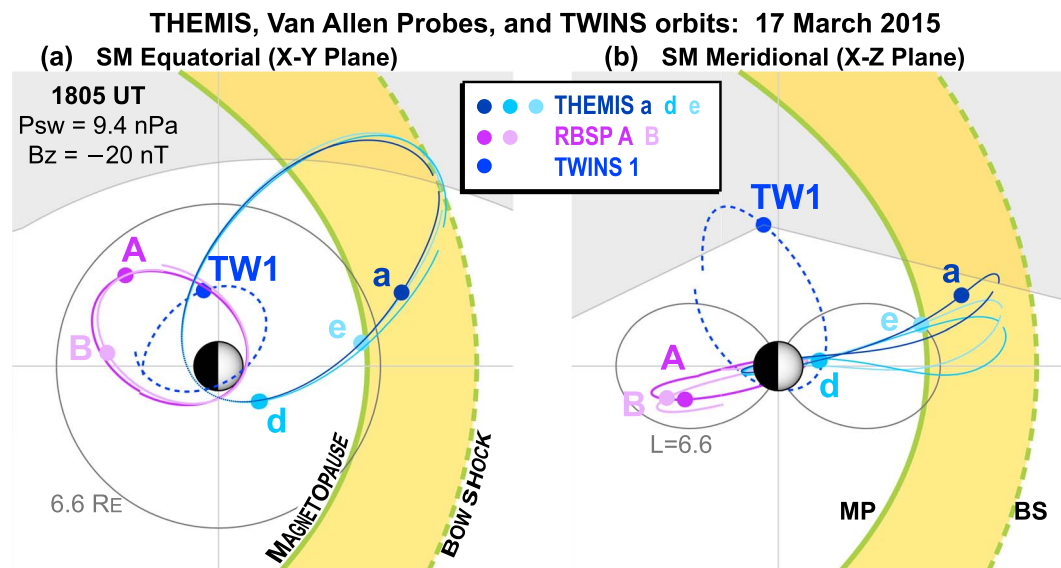
Figure 2. Orbits and locations (in solar magnetic (SM) coordinates) of three constellation missions at 1805 UT on 17 March: THEMIS, Van Allen Probes (RBSP), and TWINS. Model magnetopause and bow shock curves bound the yellow regions (see text). Gray/white areas indicate regions outside/inside TWINS 1 field of view (FOV).

The blue-gray orbits show THEMIS a, THEMIS d, and THEMIS e, which had apogees located on the dayside and orbital periods of ~1.3 days. These three spacecraft sampled the magnetosheath early in the day (section 3), and the dayside magnetosphere later in the day (section 5.5). In Figure 2, the three THEMIS spacecraft are in a "string-of-pearls" arrangement, with THEMIS a farthest out, THEMIS d closest in, and THEMIS e in the middle. Thus, although we show a THEMIS E ion spectrum once (Figure 9), in this paper we focus mostly on THEMIS a and THEMIS d data that sample the endpoints of this three-probe array.

The lavender orbits show Van Allen Probes (RBSP) A and B, which had their apogees in the premidnight magnetic local time (MLT) sector, and orbital periods of approximately 9 h. On 17 March, RBSP A and RBSP B passed through the premidnight inner magnetosphere (plasmasphere and ring current) 3 times each, with either spacecraft reaching apogee ~4 h apart.

The blue orbit depicts TWINS 1, which had its ~8 R_E apogee in the premidnight MLT sector, looking down on the magnetic equator from high northern latitude. The gray-shaded (white-colored) areas indicate regions outside (inside) the TWINS 140° field of view (FOV); the elliptical shape of the white region of Figure 2a results from the intersection of the conical FOV with the *X-Y* plane. Note that the TWINS 2 ENA imager was turned off (no science data) on 17 March 2015. Though the ENA camera recorded high levels of background noise early in the storm, TWINS 1 obtained science-quality images starting at ~1645 UT (section 5.5).

3. Initial Magnetospheric Compression

This study uses observations from three missions to track the progress of the 17 March 2015 event, from the magnetopause to the inner magnetosphere. In this section we present THEMIS multipoint local measurements that capture the magnetopause compression that initiated the storm. The in situ data are interpreted with the aid of simple models for the bow shock and magnetopause. To increase confidence in our interpretation, we validate these boundary models by direct comparison with the THEMIS data.

3.1. THEMIS Boundary Crossings
THEMIS was near its dayside apogee early on 17 March and thus observed the earliest magnetospheric compression at the start of the storm.
3.1.1. Orbit Plots
Figures 3a–3c show views of the *X-Y* (SM coordinate) equatorial plane, using a format similar to that of Figure 2a. THEMIS orbits and positions are shown at three selected times: 0440 UT, 0449 UT, and 0600 UT. The model magnetosheath (yellow area) is also shown, bounded by magnetopause ("MP") and bow shock ("BS") model curves as in Figure 2.
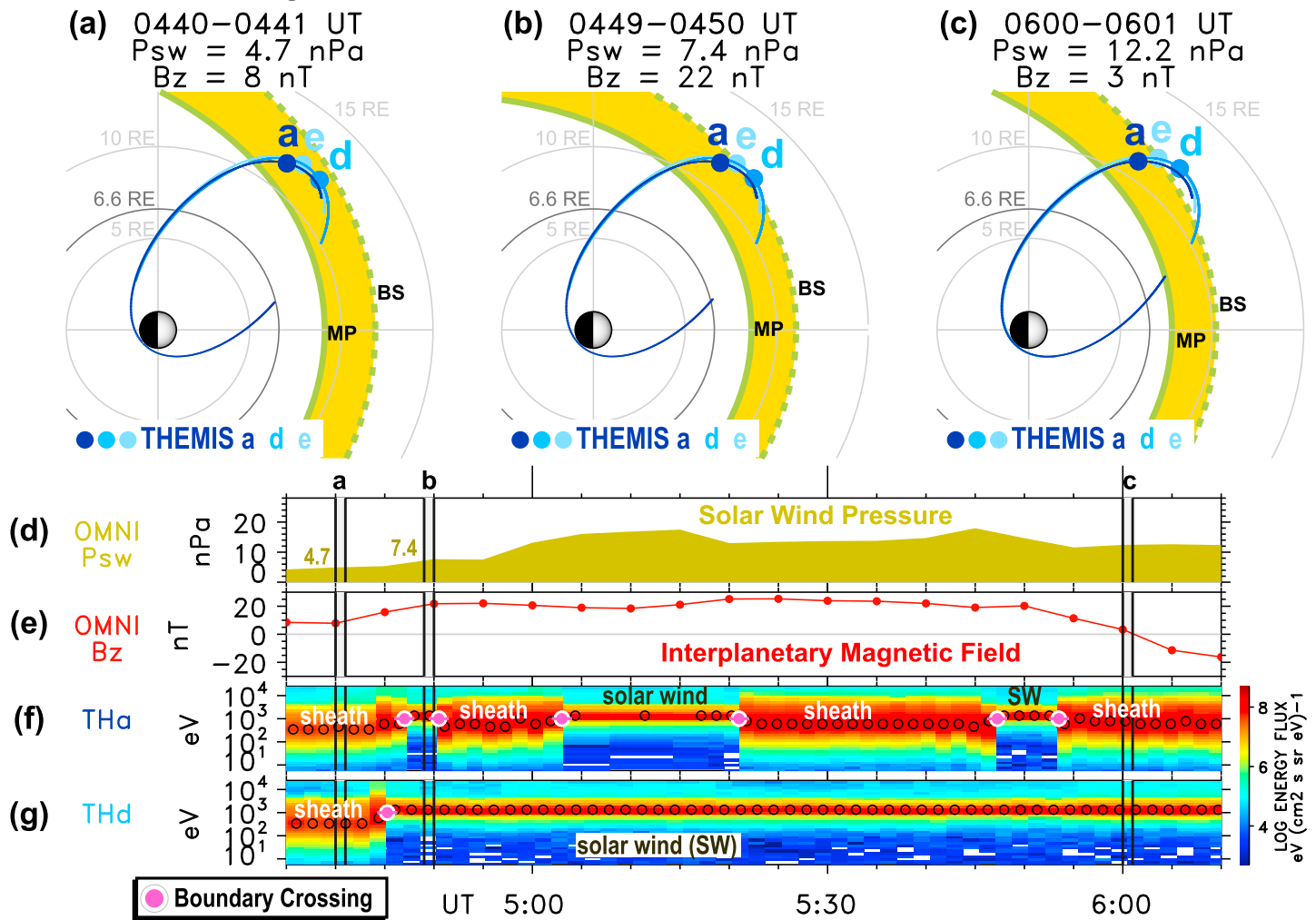
Figure 3. THEMIS observed the initial magnetospheric compression for the storm. (a and c) Orbits and locations of THEMIS a, THEMIS d, and THEMIS e are plotted in shades of blue. In each plot, light gray circles at 5, 10, 15 R_E; black circle at 6.6 R_E (geosynchronous). Model magnetopause and bow shock curves bound the yellow region. (d and e): P_{SW} and B_Z. Vertical bars ("a," "b," and "c") are times of 3 corresponding orbit plots. (f and g) Spectrograms of THEMIS energy flux. Open circles show peak energy flux value. Pink circles are boundary (magnetopause or bow shock) crossings.

3.1.2. Time Series Plots

Figures 3d through 3g are time series between 0435 and 0610 UT. Below the OMNI plots (P_{SW}, B_Z) are spectrograms of energy flux for THEMIS a and THEMIS d. (THEMIS E data during this interval are similar to THEMIS a and THEMIS d.) The vertical bars in the time series plots (labeled, a, b, and c, not to be confused with THEMIS satellite labels) indicate the times of the corresponding equatorial plots. The open circles in the spectrograms follow the time-dependent peak energy flux value. The pink circles show the times of boundary crossings, as described below.

3.1.3. THEMIS Observations

At the start of the depicted interval, all three THEMIS spacecraft were in the magnetosheath (labeled "sheath" in the spectrograms). The THEMIS a and THEMIS d spectrograms each show a broad (~100 eV – 2 keV) peak in energy flux indicating shocked solar wind ions. At 0440 UT the energy flux peak for THEMIS a (or THEMIS d) was at 0.5 keV (0.3 keV).

Between 0440 UT and 0449 UT, solar wind pressure increased by nearly 60%, from 4.7 to 7.4 nPa. This P_{SW} increase was caused mostly by a rise in solar wind speed (data not shown), from ~404 km s^{-1} to 485 km s^{-1}. As it rose, the broad energy flux peaks observed by THEMIS shifted upward, indicating higher-energy magnetosheath ions, i.e., consistent with the increased bulk flow speed of the solar wind.

At ~0446 UT, THEMIS d crossed the bow shock and entered the solar wind; this crossing is indicated by a pink circle in Figure 3g. The timing uncertainty is ±1 min, or approximately half the cadence of the THEMIS data obtained from Coordinated Data Analysis Web (CDAWeb); note the small horizontal, pink error bar. After the bow shock crossing, THEMIS d energy flux exhibited a much narrower peak at ~1 keV, consistent with the ~485 km s^{-1} solar wind speed. Soon afterward, at 0447 UT (±1 min), THEMIS a also crossed briefly into the solar wind, then back into the magnetosheath (0450 UT), as given by the pink circles (with error bars) in Figure 3f. Two more pairs of THEMIS a crossings, into and out of the solar wind, were also recorded before 0610 UT. THEMIS d remained in the solar wind until 0733 UT (±1 min), when its orbit motion (inbound from apogee) carried back into the magnetosheath. (This 0733 UT bow shock crossing is not included in Figure 3g.)

3.1.4. Boundary Model (Context)

The global boundary models [*Shue et al.*, 1997; *Jelínek et al.*, 2012] used herein provide useful context to interpret the THEMIS local measurements. Initially, as in Figure 3a, all three THEMIS probes were in the magnetosheath. The P_{SW} increase between 0440 and 0449 UT pushed the bow shock inward past the THEMIS spacecraft. THEMIS d saw the bow shock first because it was closest (in MLT) to the subsolar point where the bow shock radius is smallest (Figure 3b) and to a lesser extent because it was slightly (a few hundred km) closer to apogee. THEMIS a, at a more duskward location, spent more time skimming the (moving) boundary. The snapshot at 0600 UT (Figure 3c) illustrates this purely geometric effect: the more duskward THEMIS a was in the model magnetosheath, while THEMIS d (closer to the subsolar point) was outside the model bow shock. The 0600 UT model prediction is consistent with the spectrograms of Figures 3f and 3g, which show THEMIS a in the sheath and THEMIS d in the solar wind. However, comparing Figures 3b and 3f, the model puts the bow shock too far out at 0449 UT: the model predicts that THEMIS a was in the magnetosheath, but the data show it in the solar wind.

3.2. Model-Data Boundary Comparisons

The morphological agreement between the THEMIS ion data and the solar wind-driven boundary models, shown for the ~1.5 h interval of Figure 3, suggests that these models provide reasonably accurate contextual information to interpret the in situ data. To quantify the agreement, we recorded bow shock and magnetopause crossings for the entire day and compared them with model predictions. On 17 March 2015, THEMIS a (or THEMIS d) crossed the bow shock 12 (or 6) times and the magnetopause 2 (or 4) times. In total, there were 18 bow shock encounters and 6 magnetopause encounters.

Boundary crossings were obtained manually (as in Figures 3f and 3g), with time stamps (UT_B) rounded to the nearest 5 s. As above, the uncertainty (ΔUT_B) for each time stamp was assumed to be ±1 min (half the THEMIS data cadence).

At each crossing time (UT_B) we recorded the spacecraft geocentric distance. To assign errors resulting from the time stamp uncertainties (ΔUT_B), we recorded radius values at 3 times, $UT_B + [-1, 0, 1]\Delta UT_B$, and computed errors as $2\Delta R = R\left(UT_B + \Delta UT_B\right) - R\left(UT_B - \Delta UT_B\right)$. The resulting radial errors are generally small (on average, 0.04 R_E and maximum error of 0.2 R_E) because near apogee, the spacecraft's radius changes very little during the nominal ΔUT_B interval (i.e., ±1 min). For each crossing, we also calculated the model boundaries at the local time of the spacecraft, using the solar wind data at UT_B as inputs. To handle the two crossings that occurred during gaps in the OMNI data, we used a linear interpolation across each gap.

The result is shown in Figure 4, which plots the observed boundary locations versus the model. Plotted points are color coded by spacecraft (THEMIS a or THEMIS d), with filled circles for R_{MP} crossings and open circles for R_{BS}. The small ΔR errors are invisible in the plot. The mean difference between observed and modeled boundary locations is 0.7 R_E (indicated in the plot as dash-dotted lines). A linear fit of just the bow shock crossings (gray line in Figure 4) yields a slope of 0.3 ± 0.2 (a weak correlation). Based on this result we conclude that the models are reasonably accurate and when used carefully have provided useful global contextual information.

4. Plasmapause Motion

In the last section we described THEMIS observations of the 17 March storm's initial (~0500 UT) magnetospheric compression. In this section we present Van Allen Probes data capturing the earliest plasmapause motion resulting from the 0605 UT southward IMF turning.
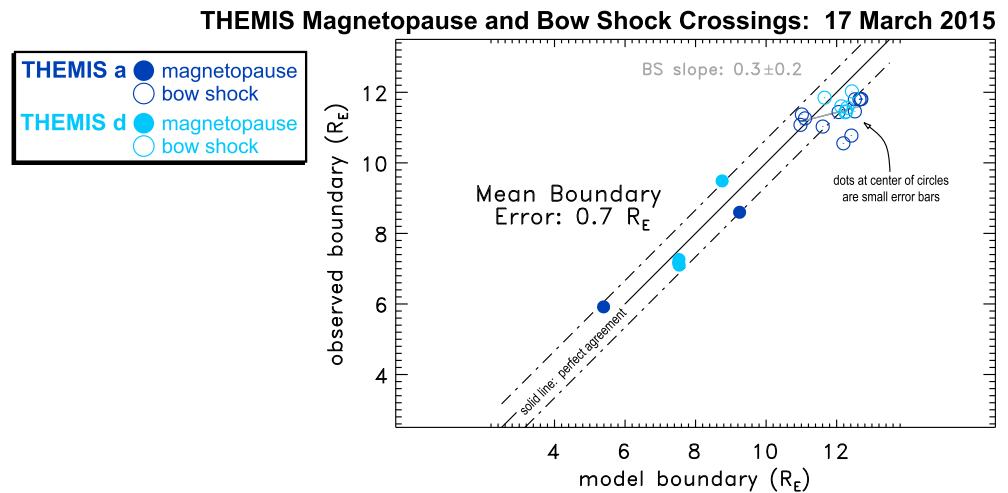
Figure 4. Comparison of THEMIS magnetopause and bow shock encounters with model predictions by *Shue et al.* [1997] and *Jelínek et al.* [2012], for 17 March 2015. Small (invisible) error bars reflect timing uncertainties in manually identified boundaries. Perfect agreement is given by the solid diagonal line. The mean error in boundary location (dash-dotted lines) is 0.7 R_E.

4.1. Plasmasphere Observations and Simulation

The plasmaspheric observations used herein are electron densities, derived from EMFISIS plasma wave data [*Kletzing et al.*, 2013; *Goldstein et al.*, 2014b; *Kurth et al.*, 2015]. These densities are extracted from the high-frequency receiver (HFR) via an automated algorithm that identifies the upper hybrid frequency and converts it to electron number density. The 5% spectral resolution of EMFISIS HFR translates to about 10% error in the extracted density values.

We employ the plasmapause test particle (PTP) simulation of *Goldstein et al.* [2014b] to provide system-level contextual information to complement the local observations. The PTP model assumes that the time-variable, global plasmapause boundary is an ensemble of $E \times B$ drifting test particles. The model calculates the boundary location only; the simulation does not provide plasma density. Particle dynamics are traced forward in time from an assumed initial condition, specified as a circular plasmapause according to the *Kp*-dependent OBM3 empirical model [*O'Brien and Moldwin*, 2003]. As discussed in *Goldstein et al.* [2014a], the PTP output is sensitive to these initial conditions; the simulation run is thus started the day before the storm to precondition the model. Preconditioning is necessary because the plasmaspheric state at a given time is determined by both the current convection field and its time history. For the 17 March 2015 simulation, the first PTP time step is 0000 UT on 16 March (i.e., 24 h before the day of interest), at which time $Kp = 1.7$, specifying an initial circular OBM3 plasmapause at $L = 5.2$. This initial state was then evolved under the influence of a model electric (E) field. The model E field is driven by solar wind data and the *Kp* index [*Goldstein et al.*, 2005a]. The output of the PTP method is reasonably accurate, on average, reproducing Van Allen Probes plasmapause locations to within 0.4 R_E. The PTP simulation has two added benefits: it is computationally inexpensive, and it preserves fine structure to a degree that would be impractical in a grid-based model.

Figure 5 compares the model with Van Allen Probes measurements during the first several hours of the storm.

4.1.1. Orbit Plots With Simulation

Figures 5a–5c are three snapshots of PTP output, plotted in the *X-Y* plane using a similar format to previous figures in this paper. In each panel, the plasmapause is the curve that bounds the green-shaded region. Also depicted in each plot are the model magnetosheath (yellow areas) and the orbits/locations of RBSP A and RBSP B.

4.1.2. Time Series Plots

Figures 5d through 5g are time series between 0120 and 0740 UT. Below the OMNI plots (P_{SW}, B_Z) are traces showing the EMFISIS-derived electron density for RBSP A and RBSP B. The vertical bars in the time series plots (labeled, a, b, and c) indicate the times of the corresponding equatorial plots.

4.2. Prestorm

At 0200 UT, the solar wind pressure was nominal (4.1 nPa) and the IMF was northward (+5 nT). EMFISIS B observed densities above 2000 cm^{-3} (Figure 5g), consistent with Probe B's near-perigee location deep within
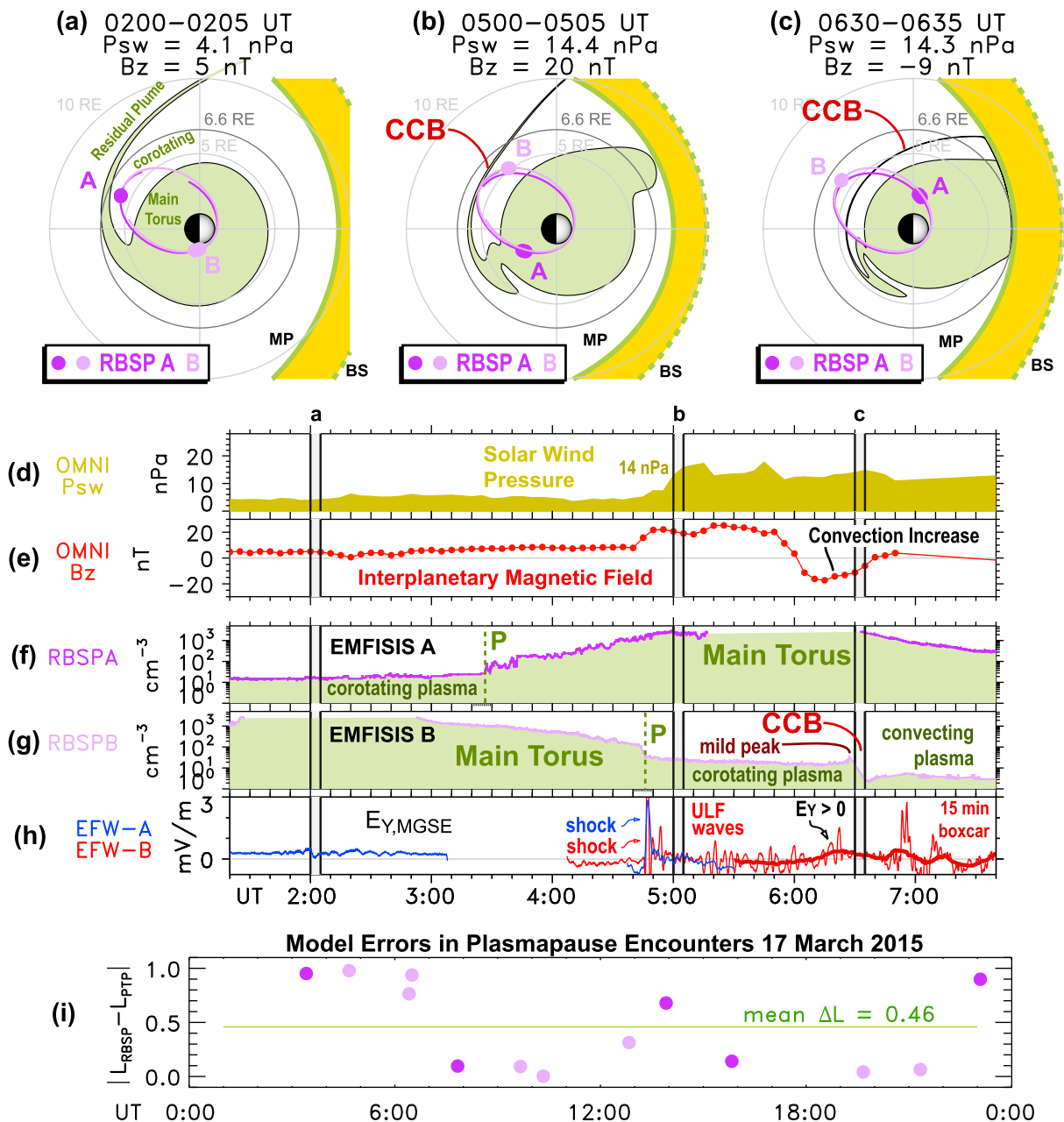
Figure 5. Van Allen Probes observed the cold plasma response to the onset of enhanced convection: in response to southward IMF the corotation-convection boundary (CCB) moved inward past Probe B. (a), (b), (c): Orbits & locations of RBSP A and B plotted (lavender). Light gray circles: 5, 10, 15 R_E. Black circle: 6.6 R_E (geosynchronous). Model magnetosheath (yellow). (d), (e): P_{SW} and B_Z. Vertical bars ('a', 'b', and 'c'): times of 3 corresponding orbit plots. (f), (g): EMFISIS-derived electron density for RBSP A and RBSP B. Step-like drop in density at ~0630 UT is the CCB. (h)EFW-measured E_Y component of electric field (cf. text). (i) Difference between observed and modeled plasmapause encounters: mean difference is 0.5 R_E.

the model plasmasphere (Figure 5a). According to the model, at 0200 UT Van Allen Probe A was located between the main torus and a residual plume [*Goldstein et al.*, 2014a, 2014b], i.e., in a region of partially depleted, corotating flux tubes. This prediction is consistent with the EMFISIS A observation of a 10–20 cm^{-3} plateau at this time (Figure 5f).

4.3. Plasmapause Crossings and SSC

After 0200 UT Probe A moved inbound from apogee. At 0327 UT, EMFISIS A recorded a steep transition to >50 cm^{-3} ("P" in Figure 5f), which we interpret as entry into the main torus. In the PTP model, Probe A transited

the boundary 48 min later, at 0415 UT. During the same time period Probe B was outbound from perigee. At 0446 UT EMFISIS B recorded a steep drop from >100 to <30 cm^{-3} (P in Figure 5g), indicating a crossing from the main torus to the region of partially depleted, corotating flux tubes. In the PTP model, Probe B crossed the plasmapause 36 min earlier, at 0410 UT. Timing errors in model plasmpause encounters are worth a brief examination. Following *Goldstein et al.* [2014b], we manually extracted plasmapause encounter L values for 17 March 2015. Figure 5i plots the data-model difference $\Delta L_P = |L_{RBSP} - L_{PTP}|$. The mean ΔL_P is 0.5 R_E, which is 25% higher than the 0.4 R_E mean error found on the dawnside by *Goldstein et al.* [2014b]. Larger errors on the duskside (where more complex density structures reside) are not surprising, although this higher ΔL_P may not be physically significant.

By 0500 UT Probe A was well inside the plasmasphere, and Probe B had recently exited the main torus into the depleted corotation region, as shown in both the model plot of Figure 5b and the EMFISIS densities of Figures 5f and 5g. At this time (0500 UT) the storm sudden commencement (SSC) was underway, triggered by the P_{SW} increase to ∼14 nPa (Figure 5d). Though this P_{SW} increase compressed the magnetopause and bow shock inward (Figure 5b), it appeared to have no significant impact on the plasmasphere, according to both model and data. The lack of P_{SW}-driven effects is expected for the model. Because the model assumes a static dipole magnetic field, it is largely insensitive to solar wind pressure, except to the extent to which Kp (one of the model's drivers) might reflect P_{SW} variability. The differences between the model snapshots at 0200 UT (Figure 5a) and 0500 UT (Figure 5b) appear entirely attributable to the very weak convection driven by the northward IMF recorded during the intervening 3 h. Consistent with the model, the EMFISIS densities also show no evidence of a P_{SW}-driven effect. During the interval of steepest P_{SW} increase, there was no discernable associated change in measured electron density (Figures 5f and 5g).

4.4. Convection Onset

According to the PTP model, at the start of the storm there was a residual plume wrapped around the main torus, on the nightside. Such residual plumes demarcate the corotation-convection boundary (CCB), i.e., the boundary between corotating and convecting flux tubes [*Goldstein and Sandel*, 2005; *Goldstein et al.*, 2005c]. Enhanced convection moves the CCB inward, bringing residual plumes (and other corotating density structures) with it.

At 0605 UT the IMF turned southward ($B_Z < -10$ nT; cf. Figure 5e), initiating enhanced convection. Consequently, the PTP model's residual plume and CCB were carried sunward, i.e., inward past Van Allen Probes B (Figure 5c). In the simulation, Probe B crossed into the convection region at 0615 UT. In the data (cf. Figure 5g), EMFISIS B measured first a mild density peak beginning at ∼0620 UT, then a step-like drop in density, from ∼30 to 2 cm^{-3}, during 0628–0635 UT. We interpret this density step as the moving CCB, based on two factors. First, the PTP model predicts that the CCB convected past Probe B at approximately the time of the observed density step. Second, the mild peak in density is morphologically similar to the detached plasma recorded by EMFISIS during the January 2013 event study [*Goldstein et al.*, 2014b] and also found to roughly coincide with the location of a modeled wrapped, residual plume. That is, the mild peak occurs near the outer edge of a 10–20 cm^{-3} density plateau and resembles the signature of a residual plume.

Based on this comparison of the PTP simulation output and EMFISIS density data, we conclude that Van Allen Probes B captured the earliest onset (on the nightside) of enhanced sunward convection during the 17 March storm and that the global plasmasphere morphology predicted by the model is probably correct to within 0.5 R_E.

Van Allen Probes electric field measurements are available for this storm, from the Electric Field and Waves (EFW) suite [*Wygant et al.*, 2013]. EFW measurements are shown in Figure 5h for Van Allen Probes A (blue) and B (red); these traces plot the E_Y component in modified GSE (MGSE) coordinates [*Wygant*, 2013]. In the MGSE coordinate system positive E_Y points approximately duskward. Only data with good quality flags are included in the plot. The bold maroon curve is a 15-min boxcar average of the EFW-B data.

Just before 0450 UT there was a strong (several mV/m) spike recorded by both Van Allen Probe A (inside the postmidnight plasmasphere, $L < 4$) and Probe B (closer to dusk, outside the main plasmaspheric torus). These simultaneous measurements at two disparate locations are evidence of a solar wind shock (steep jump in solar wind speed from ∼400 to >500 km s^{-1}) that struck the magnetosphere [*Kanekal et al.*, 2016]. After the shock, Probe B (and to a lesser extent, Probe A) measured ultralow frequency (ULF) wave activity in the ∼3–6 min periodicity (2.8–5.6 mHz) range, consistent with global magnetospheric "ringing" after the shock.

After 0530 UT the EFW-A data (from near perigee) are not shown because these low-L measurements include uncorrected attitude errors that propagate to an imperfect subtraction of the $v \times B$ associated with the spacecraft motion. At about 0600 UT the initial southward B_Z turning occurred (Figure 5e). Approximately 20–30 min later Probe B recorded a mild (<1 mV/m) positive bias in E_Y. At ~ 0650 UT Probe B (near apogee in the premidnight MLT sector) measured a ~2 mV/m rise in E_Y followed by sub-1 mHz oscillations. Though not unequivocal evidence of convection, these later $E_Y > 0$ signals are consistent with the establishment of global magnetospheric convection via propagation of reconnected field lines from the dayside to the nightside [*Coroniti and Kennel*, 1973; *Goldstein and Sandel*, 2005; *Thaller et al.*, 2015].

5. Ring Current Dynamics

We now study in situ ring current ion observations (mostly Van Allen Probes but some THEMIS), using both the PTP simulation and TWINS imaging data for global context. First, we introduce our data plots in section 5.1, and then we interpret the data. Van Allen Probes captured the prestorm ring current (section 5.2), the energetic ion response to the onset of enhanced convection (section 5.3), and multiple injections during the first few hours of the storm (section 5.4). In section 5.5 we combine data from all three missions (THEMIS, Van Allen Probes, and TWINS) to study the main phase of the storm. Section 5.6 uses Van Allen Probes and TWINS data to study a midstorm injection.

5.1. Van Allen Probes HOPE Observations

Figure 6 depicts the same interval (0120 to 0740 UT) as Figure 5, but with the addition of RBSP A and B HOPE proton (H^+) data. Whereas Figure 5 focused on the cold plasma dynamics in response to the convection onset, Figure 6 focuses on the ring current dynamics during the same time period. The repetition of some information from Figure 5 is for the convenience of the ring current discussion. Figures 6a–6c are three snapshots of PTP output as in Figure 5. Below each PTP plot is a corresponding HOPE proton spectrum (flux versus energy) obtained at the location of one of the Van Allen Probes spacecraft. (Note that the panel labels a, b, and c are repeated in the equatorial and spectrogram plots.) Each H^+ spectrum is labeled with its L and MLT locations and indicates which probe (A or B) made the measurement. The large amount of scatter in fluxes at lower energies (<1 keV) reflects lower count rates (i.e., counting statistics) in this energy range; note that for the HOPE instrument count rate is proportional to energy flux, not flux. Figures 6d through 6i are time series between 0120 and 0740 UT. The OMNI and EMFISIS plots are the same as Figure 5. Two new plots (Figures 6f and 6g) show HOPE A and HOPE B proton spectrograms (flux versus energy and time). As before, the vertical bars in the time series plots (labeled, a, b, and c) indicate the times of the corresponding equatorial plots.

Figure 8, discussed later (cf. section 5.4), repeats the format of Figure 6 for the interval 0600 to 1030 UT.

5.2. Prestorm and SSC

As discussed in section 4, prior to the storm, Van Allen Probes A was located in the region of corotating flux tubes, between the main plasmasphere torus and a residual plume. At 0200 UT, Probe A was within this corotating zone at $L = 5.7$ and 2229 MLT and measured a proton flux spectrum with peaks at ~2 keV and 6 keV (Figure 6a). This two-peak structure was stable, lasting from the start of the day through about 0418 UT (cf. red-orange linear features labeled with black arrows, Figure 6f), although the energies of the peaks varied somewhat (as discussed below). In particular, after Probe A crossed the plasmapause (at about 0327 UT; cf. Figure 6h), the ~2 keV peak fell in energy, to <1 keV by 0410 UT. This falling energy signature may be a proton version of the "trunk-like" spectral feature found in He^+ and O^+ by *Zhang et al.* [2015], as discussed in the penultimate paragraph of this section. As Van Allen Probe B emerged from the main plasmasphere torus at 0446 UT (Figure 6i), it also recorded a similar two-peak spectrum; see, for example, the two peaks (~2 keV and 9 keV) in the proton spectrum of Figure 6b, measured at 0500 UT ($L = 5.1$, 2034 MLT). As was the case for Probe A, the two peaks observed by Probe B were stable (though they varied in energy), lasting until enhanced convection began at 0620 UT.

This type of narrow ring current peak, known as a nose structure, was first identified in Explorer 45 data [*Smith and Hoffman*, 1974; *Ejiri et al.*, 1980] and is a familiar feature in data from both Van Allen Probes and Cluster [*Ferradas et al.*, 2014, 2015, 2016; *Burke et al.*, 2016]. The stable, two-peak spectrum observed by both Van Allen Probes on 17 March, the so-called double nose, has also been previously observed [e.g., in Cluster data by *Vallat et al.*, 2007]. Though not entirely understood, nose spectra are thought to be generated by a combination of distinct drift physics and source processes [*Buzulukova et al.*, 2002, 2003; *Vallat et al.*, 2007; *Ferradas et al.*, 2015]. The most commonly accepted explanation involves the existence of a limited band of energies
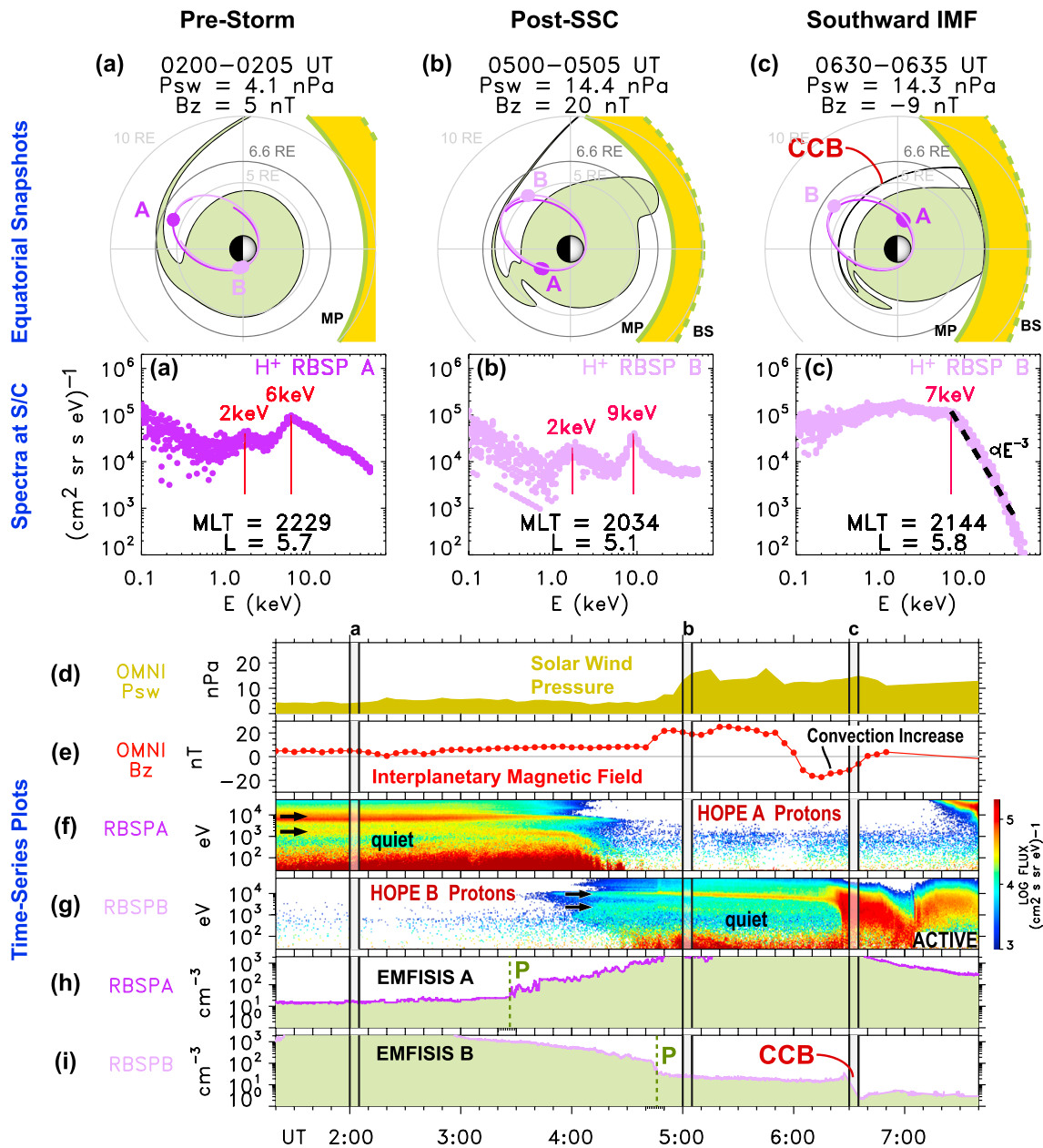
Figure 6. Van Allen Probes also observed the ring current response to onset of enhanced convection. This figure shows the same orbit snapshots and interval as Figure 5, with the addition of RBSP HOPE spectra and spectrograms. (a and c) Beneath each orbit plot is a HOPE proton spectrum (flux versus energy) at the location of Van Allen Probe A or B. (d and e) P_{SW} and B_z. (f and g) HOPE proton spectrograms (flux versus energy and time). After convection increase, HOPE observed newly injected ring current ions outside the CCB. (f and g) EMFISIS-derived electron density (RBSP A and RBSP B).

for which the convective and magnetic drifts essentially cancel. In this energy band, the absence of significant azimuthal drifts permits the deeper penetration of ions to lower L values and into the plasmasphere. This penetration produces the characteristic nose signature: a band of enhanced ion flux that is narrower at low L and broadens with increasing L. The double nose is believed to occur when a stagnation dip (again, from roughly equal and opposite convective and magnetic drifts) is created within the nose energy band. Ion nose structures were first identified by *Smith and Hoffman* [1974] as a storm time feature at lower L ($L \approx 4$ to 5). Many subsequent observations have determined that stationary nose structures appear regardless of magnetospheric activity level—even during extremely quiet conditions—and at higher L values ($L \approx 6$ to 7) [*Vallat et al.*, 2007; *Ferradas et al.*, 2015, 2016].
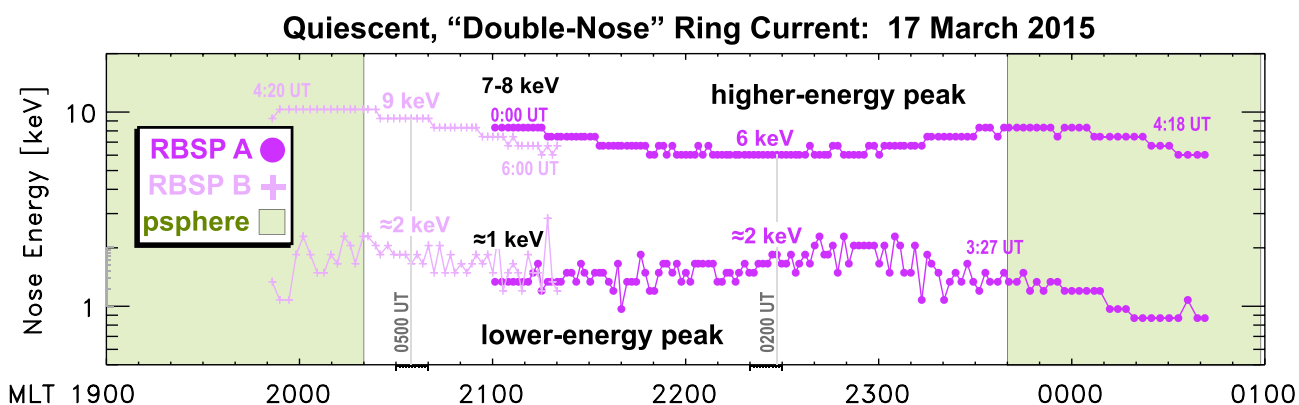
Figure 7. Energy of ring current double-nose features [*Buzulukova et al.*, 2003; *Vallat et al.*, 2007] in Van Allen Probes HOPE proton spectra, 0000 UT to 0600 UT on 17 March 2015.

To characterize these double-nose spectra, the two peaks were automatically extracted from HOPE (A and B) spectrograms, at a 2 min cadence between 0000 UT and 0600 UT on 17 March. The automated algorithm searches for a local maximum in each of two custom ranges: 0.8–3 keV for the lower energy peak and >3 keV for the higher-energy peak. The result is shown in Figure 7. Moving inbound from apogee, Probe A (dark lavender) observed the two peaks between 2100 MLT and 0040 MLT, during 0000–0410 UT. Traveling outbound, Probe B (pale lavender) observed the double-nose spectra between 1950 MLT and 2120 MLT, during 0420–0600 UT. For reference in the following discussion, the plasmaspheric region (section 4) is shaded light green.

It is remarkable that near 2100 MLT, Probes A and B measured extremely similar double-nose peaks (∼1 keV and 7–8 keV) even though these two measurements were made approximately 6 h apart. Given that the double-nose energies varied along the A and B orbits, the similarity of the Probes A and B spectra from 2100 MLT suggests that the double-nose ring current may be a stable (or even static) structure whose energy simply varies with MLT.

The energy variation is worth a brief examination. The more energetic peak falls gently from 10 keV at 2000 MLT to a broad minimum of 6 keV spanning 2200–2300 MLT then rises to a broad 8 keV maximum centered roughly at the plasmapause. The lower energy peak has a broad minimum at ∼1 keV between 2100 and 2200 MLT, bracketed by 2 keV regions at 2020 and 2250 MLT. It is interesting that the lower peak's energy falls with increasing penetration into the plasmasphere, west of 2020 MLT and east of 2340 MLT. This falling energy signature, dubbed trunk-like (for its resemblance to an elephant's trunk), was previously observed in heavy ions (He^+ and O^+) by *Zhang et al.* [2015] but not protons. We speculate that inside the dense plasmasphere, ring current protons are subject to Coulomb collisions leading to energy degradation [*Fok et al.*, 1991, 1993]. More evidence for the influence of Coulomb-scattering energy degradation may be found in the buildup of flux at sub-keV energies (cf. spectra of Figures 6a and 6b), observed on drift paths containing at least 10 cm^{-3} of cold plasma.

We conclude this subsection by noting that as with the cold plasma observations during the SSC (section 4), the HOPE proton data of Figure 6 show no evidence of changes associated with the steep rise in P_{SW} around 0500 UT.

5.3. Convection Onset

Shortly after the IMF turned southward and convection increased (Figure 6e), Probe B crossed the CCB (Figure 6i). At the CCB, the measured protons exhibited an abrupt transition from stable/quiescent to active. By ∼0630 UT (Figure 6c) the double-nose spectrum had been replaced by a single, broad peak with a fivefold increase (compared to the nose spectra) in maximum flux. Below 7 keV the spectrum is relatively flat. Above 7 keV the spectrum falls off steeply, approximately ∝ E^{-3} (cf. dashed line in Figure 6c).

Our interpretation is that the post-0630 UT spectrum reflects a new plasma injection triggered by the increased convection. The 0605 UT southward turning (Figure 6e) initiated new dayside magnetopause reconnection. Approximately 15 min later, enhanced sunward convection was observed in the nightside inner magnetosphere: the CCB convected past Probe B (according to the PTP model; cf. section 4), and the earliest
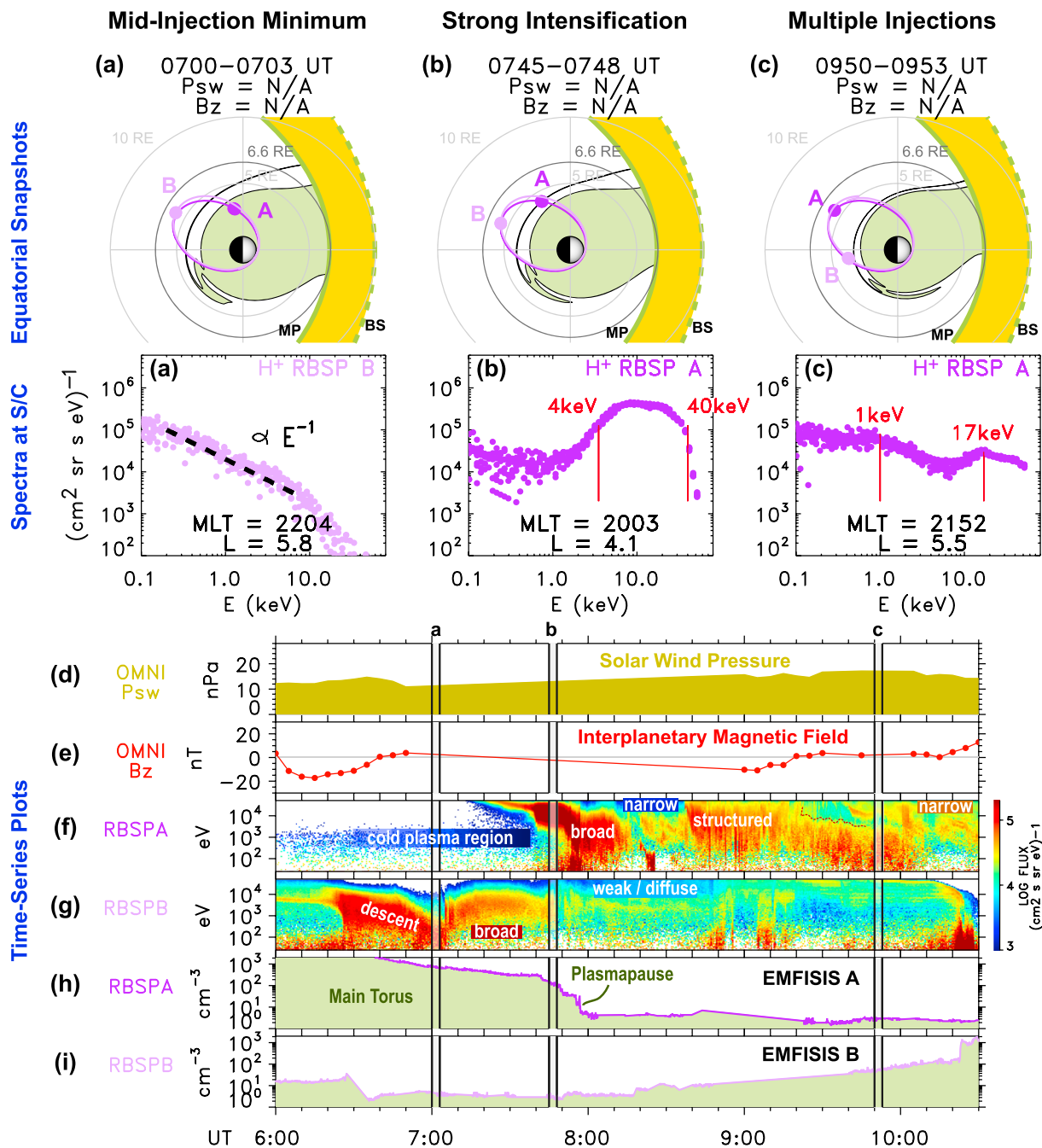
Figure 8. During the first few hours of the storm (0600 to 1030 UT)), Van Allen Probes recorded multiple injections in a highly dynamic ring current. The format of this figure is identical to that of Figure 6. Because the equatorial snapshots (a, b, c) are at times during OMNI data gaps, the model magnetosheath uses interpolated P_{SW} and B_Z values.

rise in proton flux was observed. Dayside-to-nightside time delays of ~10–30 min are not uncommon [e.g., *Goldstein et al.*, 2003, 2005c; *Goldstein and Sandel*, 2005]. In the PTP model, the enhanced convection caused further inward motion of the nightside plasmapause (Figure 8).

5.4. Early-Storm Dynamics: Multiple Injections

With enhanced convection underway, the first several hours of the 17 March 2015 storm witnessed a highly dynamic ring current. After the intense, energetic, broad spectral peak observed by Probe B at 0630 UT (Figure 6c), the measured proton peak energy dropped to a sub-keV minimum by 0700 UT. This rapid descent in energy is visible in the spectrogram of Figure 8g. The minimum-energy spectrum at 0700 UT approximately

follows an E^{-1} dependence (Figure 8a). After the energy minimum at 0700 UT the proton flux peak shifted back upward in energy, recovering a broad and energetic spectral peak by 0720 UT. This peak then dissipated and after 0800 UT was succeeded by over 2 h of weak/diffuse, variable proton spectra (in the HOPE energy range).

While deep inside the plasmasphere (prior to 0700 UT), Probe A saw no ring current protons in the HOPE energy range (Figure 8f), although in this region significant ion fluxes were recorded by the MAGEIS instrument at higher (several hundred keV) energies (MAGEIS data for this interval found at http://cdaweb. gsfc.nasa.gov/). As the spacecraft moved through the outer plasmasphere (0720–0740 UT), a narrow, nose-like spectrum was observed, with peak energy falling from the upper limit of HOPE's range to about 30 keV by 0735 UT. Probe A transited the plasmapause density gradient during 0740–0800 UT (cf. PTP simulation of Figure 8b and EMFISIS density of Figure 8h). During this transit, HOPE A recorded a sudden, strong intensification of proton flux in a broad energy range spanning 4 keV to 40 keV (Figure 8b). In the cold plasma region, ring current protons are mostly excluded, except at the highest energies.

Once outside the plasmasphere, during 0800 UT to 1030 UT, Probe A measured many injections, having a prodigious variety of different spectral shapes (Figure 8f). A broad, several-keV peak appeared during 0800–0810 UT. Then narrow, rapid, several-keV injections (0820–0838 UT) were followed by energetic, temporally structured peaks (0838–0920 UT), whose upper edge fell abruptly to the few-keV range after 0924 UT. After 0940 UT these broad but less energetic spectra were augmented by narrow/nose-like peaks in the tens-of-keV range. A snapshot from this period (Figure 8c) contains a broad, low-energy peak (1 keV) and a more narrow 17 keV peak. These spectra with multiple peaks persisted for many minutes. After 1014 UT the low-energy peaks vanished, leaving behind a narrow peak in the keV range.

The Van Allen Probes spectrograms illustrate a feature of this strong geomagnetic storm: The degree of both temporal and spatial structure. There were rapid changes in both the intensity and energy of early-storm proton injections sampled by Probe A. Meanwhile, just a few MLT hours east of this vigorous series of injections, Probe B observed only weak and diffuse proton signatures. We also note (without showing the data herein) that EMFISIS observed a plasma wave environment that was every bit as dynamic as the proton spectra.

5.5. Storm Main Phase

In this section we use the three-mission constellation to study the main phase of the 17 March 2015 storm.

5.5.1. Plots for Cross-Scale Analysis

Figure 9 is similar in format to Figure 6 (or Figure 8) but with the addition of THEMIS and TWINS observations to interpret alongside those of the Van Allen Probes.

Figures 9a–9c are snapshots of the models (PTP and magnetosheath), as before. Orbits/locations of RBSP (A and B) and THEMIS (a, d, and e) are overplotted together. Added to Figure 9c is a map of TWINS 1 ion flux, obtained via numerical inversion [*Perez et al.*, 2012, 2016] from the nearest-in-time (1645 UT) ENA image. The TWINS inversion map shows 15 keV pitch angle-averaged equatorial flux in units of $\log_{10}(\text{cm}^2\,\text{sr}\,\text{s}\,\text{eV})^{-1}$, as given by the colorbar at the bottom right. Below each equatorial plot are spectra (flux versus energy) of RBSP A protons and THEMIS ions, at the corresponding locations shown in the orbit plot. The THEMIS flux spectra were converted from energy flux by dividing out the ion energy. The (L, MLT) label at the bottom of each spectrum refers to position used to sample both RBSP A and TWINS data but not THEMIS (which is sampled at a different location). The spectrum in Figure 9c also includes TWINS 1 flux, derived from inversion maps at a series of energies (from 5 to 65 keV) similar to the one shown in the equatorial plot above it.

Figures 9d through 9i are time series between 1130 and 1700 UT. Figures 9d and 9e contain spectrograms of THEMIS (a and d) ion energy flux. Figures 9f and 9g show RBSP A and RBSP B (HOPE) proton flux spectrograms. Figures 9h and 9i contain EMFISIS density plots.

5.5.2. Midnight Ring Current Buildup

A rotation of the IMF from northward (+18 nT at 1140 UT) to southward (−6 nT by 1200 UT and −27 nT by ~1300 UT; cf. Figure 1a) initiated half a day of strong, sustained convection. This transition caused severe erosion of the PTP model plasmasphere (Figure 9c) and also set in motion a major buildup of the ring current.

Figure 9a shows that the RBSP A proton spectrum at 1145 UT ($L = 5.2$, 2311 MLT) had a peak at ~20 keV. About 5 MLT hour west but at the same L value, THEMIS a recorded a spectrum with the suggestion of a >10 keV peak but with 50 times lower flux. Over the next hour, the ring current intensified. As shown in the RBSP A
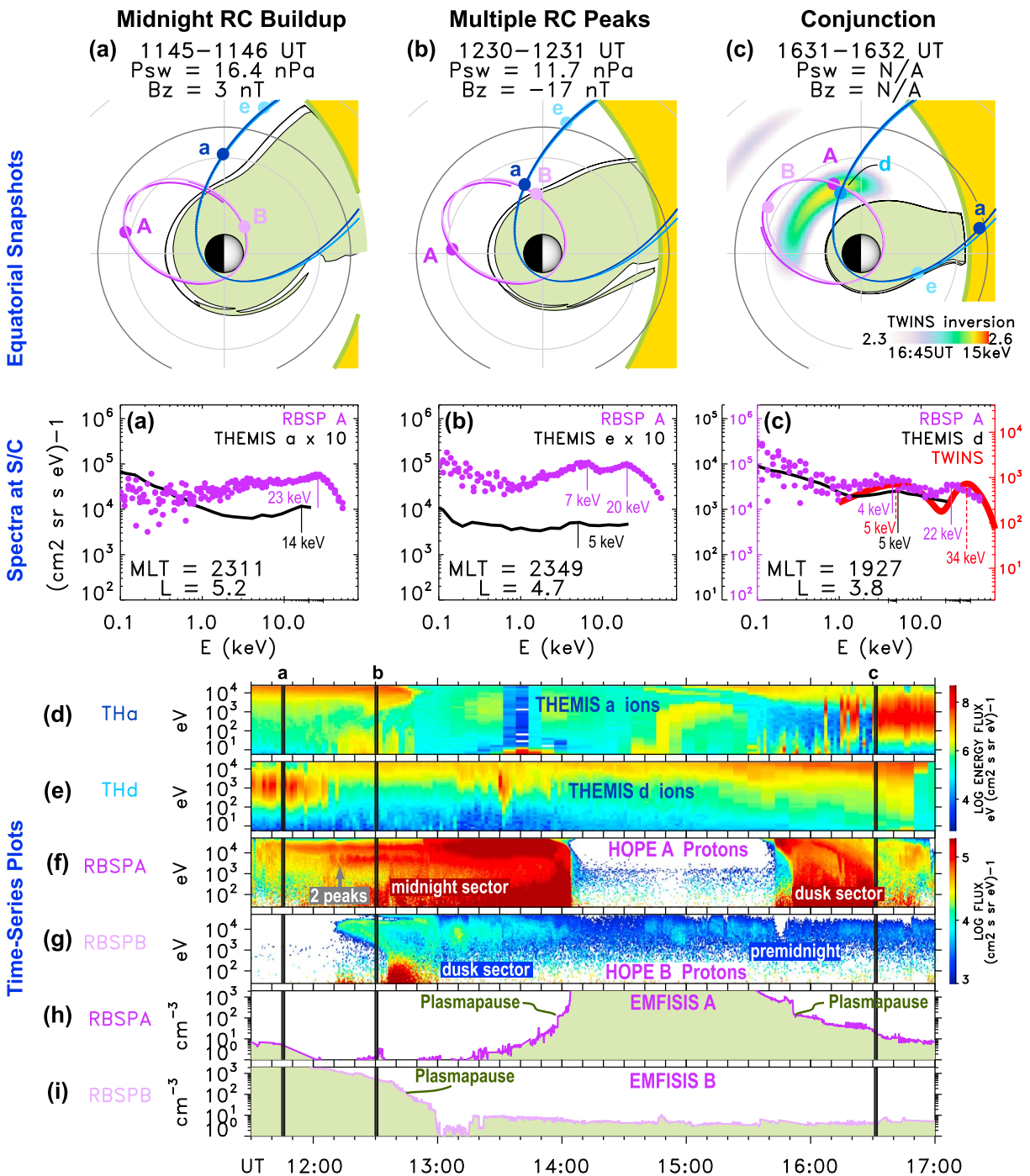
Figure 9. Van Allen Probes, THEMIS, and TWINS observations during main phase of 17 March 2015 storm. (a–c) Three equatorial plots (1145, 1356, 1631 UT) show locations/orbits of RBSP (A and B) and THEMIS (a, d, and e). Snapshot at 1631 UT adds global TWINS 1 (15 keV) ion flux. Beneath each orbit plot, single-point spectra from RBSP/HOPE (lavender), THEMIS (black), and TWINS (red). (d and e) THEMIS (a and d) spectrograms (energy flux versus energy and time). (f and g) HOPE proton spectrograms (flux versus energy and time). (h and i) EMFISIS-derived electron density (RBSP A and RBSP B). In the spectrum plot of Figure 9c the flux scales (ordinate axis) are color coded: black for THEMIS, lavender for Van Allen Probes, and red for TWINS.

spectrum of Figure 9b, by 1230 UT ($L = 4.7$, 2349 MLT) the flux in the 20 keV peak had doubled. The spectrum also developed a second peak at lower energy (7 keV), perhaps evidence of fresh plasma brought earthward by the recently enhanced convection. At $L = 7$ near dusk, THEMIS e observed a flat, weak spectrum with the suggestion of a 5 keV peak. These measurements during 1145–1230 UT indicate that fluxes were consistently higher near midnight than near dusk. During 1230–1400 UT, RBSP B exited the duskside plasmapause and

likewise saw consistently lower fluxes (Figure 9g) than RBSP A. Thus, Van Allen Probes and THEMIS multipoint observations reveal that between ~midday and ~1400 UT on 17 March, the global peak of the partial ring current (RC) was closer to midnight than dusk.

At ~1300 UT, RBSP A crossed the midnight meridian. At this time HOPE A began measuring a buildup of flux at high energies (>10 keV), indicating either that hotter ring current protons were freshly injected or that Probe A entered an existing region of hotter protons. These observations are also consistent with a global RC peak closer to midnight than dusk and indeed might even indicate that the RC peak was skewed slightly east of midnight.

5.5.3. Spectra at the Peak of the Partial RC

Figure 9c (orbit plot) shows a close conjunction of the three missions at 1631 UT. Van Allen Probes A was at ($L=3.8$, 1927 MLT) and THEMIS d was at ($L=3.4$, 1914 MLT). From the TWINS ion flux map, the global peak of the partial RC was at ($L=3.6$, 1938 MLT). That is, both RBSP A and THEMIS d were close to the global RC peak, and this conjunction is therefore an opportunity for a direct comparison of flux spectra from the two in situ measurements plus the nearest-in-time TWINS global image.

The absolute fluxes disagree among the three measurements. In the spectrum plot of Figure 9c the flux scales (ordinate axis) are color coded: black for THEMIS, lavender for Van Allen Probes, and red for TWINS. The THEMIS flux levels are 10 times smaller than those measured by Van Allen Probes but 5 times greater than those of TWINS. The disagreement between TWINS and the two in situ measurements can be partially explained by the fundamental difference between in situ versus ENA-derived global flux. On one hand, we expect (and THEMIS and Van Allen Probe missions have confirmed) that ion flux distributions contain sharp spatial gradients that are dynamic over time. On the other hand, the TWINS ion fluxes are derived from ENA fluxes averaged over the camera's finite intrinsic angular resolution of >1°, corresponding to >1 R_E when projected to the equator from TWINS' 7.2 R_E apogee. Furthermore, each TWINS pixel samples multiple L shells; i.e., measured ENA flux includes contributions from all along a given line of sight (LOS) through the distribution of ENA emission sources. TWINS-derived ion fluxes thus represent the average emission from a source volume larger than the in situ-observed spatial gradients. This factor leads to an inevitable blurring of these fine structures and flux extremes; consequently, the ENA-derived ion flux at a given location can be lower than the in situ measured flux at that same location [*Vallat et al.*, 2004; *Perez et al.*, 2012, 2015; *Valek et al.*, 2015].

However, it is noteworthy that the two different in situ measurements (THEMIS and RBSP) differ from each other by an order of magnitude. This inequality might be attributed to at least two factors. First, the measurements were at slightly different locations (separated by 0.4 R_E). Second, it can be difficult to cross-calibrate instruments on different spacecraft (or missions) or even on the same spacecraft. Indeed, fluxes measured by a different instrument (Radiation Belt Storm Probes Ion Composition Experiment (RBSPICE)) on the same spacecraft (RBSP A), obtained during the same 17 March storm, are significantly lower than those measured simultaneously by HOPE. For example, between 1700 and 1715 UT RBSPICE A measured a peak 30 keV flux of ~300 (cm² sr s eV)⁻¹ [*Perez et al.*, 2016]. In the same interval, HOPE A recorded a mean 30 keV flux of 6×10^3 (cm² sr s eV)⁻¹, i.e., >20 times higher flux. Thus, while it is common to treat the ENA-derived fluxes as subject to validation by "ground truth" in situ measurements [*Vallat et al.*, 2004; *Perez et al.*, 2012], the disagreement in local flux values raises questions about this interpretation. It is perhaps more realistic to state that the plot of Figure 9c simply contains three different measurements of absolute flux.

Despite the disparity in absolute flux, the shapes of the three measured spectra are in good qualitative agreement. RBSP A (lavender spectrum) saw an E^{-1} dependence below ~1 keV and peaks at 4 keV and ~20 keV. Within its energy range the THEMIS d spectral shape agrees with RBSP A: an E^{-1} sub-keV dependence and a peak at 5 keV. The TWINS spectrum (red) has peaks at 5 keV and ~30 keV. Taken together, the three measurements indicate that the 1631–1645 UT spectrum at the global RC peak followed an E^{-1} dependence below 1 keV and had two peaks: one at 4–5 keV and the other at 20–30 keV.

5.5.4. Did the Partial RC Migrate Westward?

According to the TWINS flux map of Figure 9c, at 1645 UT the partial RC spanned the premidnight MLT quadrant, with the highest flux levels between 1900 and 2100 MLT. That is, at this time the global peak of the partial RC was closer to dusk than midnight. This situation represents an evolution from that of just a few hours prior (as late as 1400 UT), when RBSP A (near midnight) saw order-of-magnitude higher flux levels than RBSP B (near dusk) did. The MLT location of the ring current ion flux peak depends on energy, epoch time, and storm time dynamics. Whereas traditional solar-wind-driven convection models [e.g., *Weimer*, 1996] put the
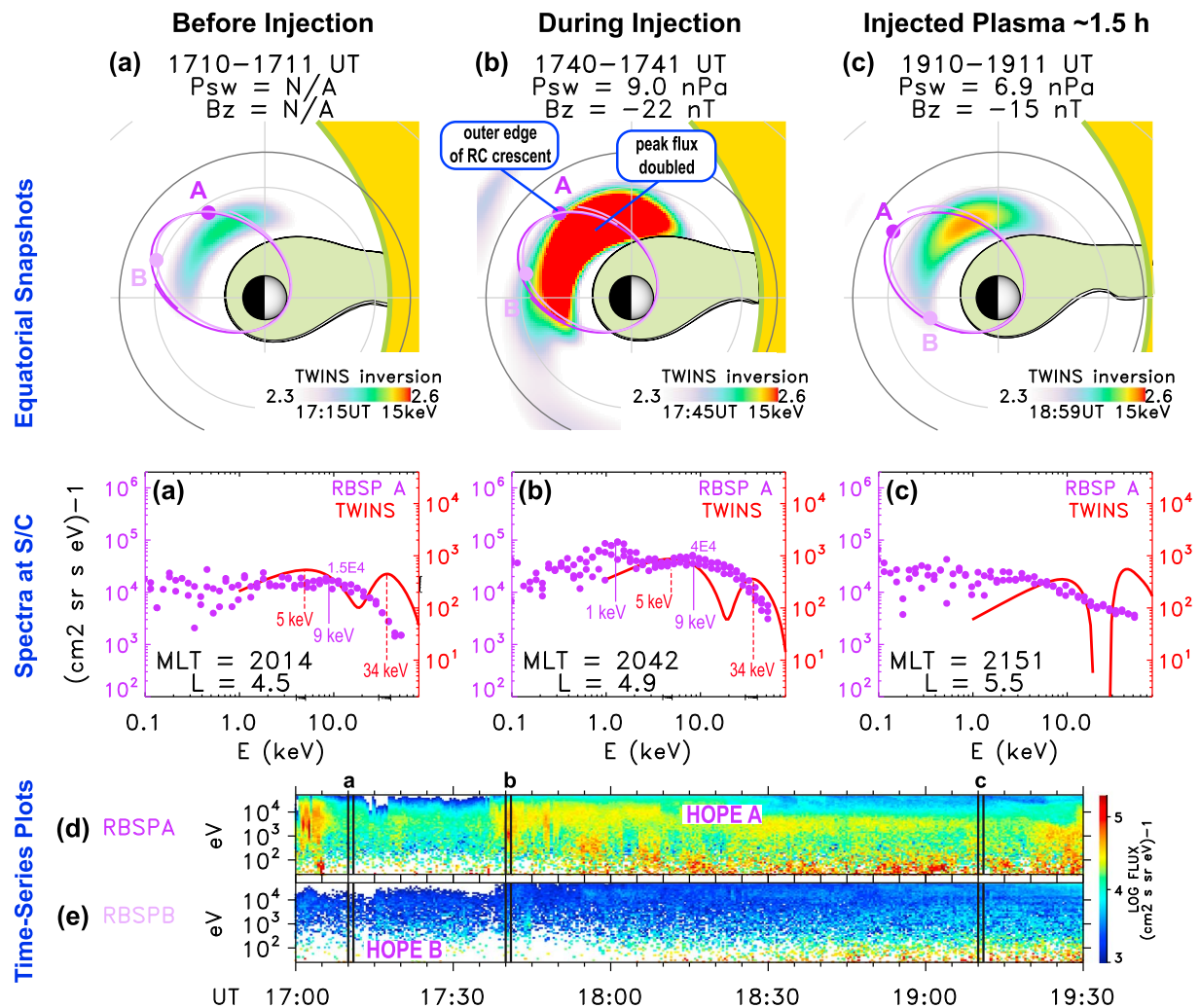
Figure 10. Van Allen Probes and TWINS observations of isolated injection at 1740 UT. (a–c) Three equatorial views (1710, 1740, 1910 UT) of RBSP (A and B) orbits and locations, and TWINS 1 global (15 keV) ion flux. Beneath each snapshot, single-point spectra from RBSP/HOPE (lavender) and TWINS (red). Each spectrum plot has two color-coded vertical axes of absolute flux values for RBSP and TWINS. (d and e) HOPE proton spectrograms (flux versus energy and time). Note the color-coded flux scales (ordinate axis of plot) for RBSP and TWINS.

ring current peak closer to dusk, ENA imaging, and self-consistent treatments of convection — involving ring current-ionosphere (RC-I) coupling/feedback — have shown ring current peaks skewed into the postmidnight sector [*Brandt et al.*, 2002; *Fok et al.*, 2003; *Burch*, 2005]. Migration of the ring current from midnight toward dusk might therefore represent a modification of the RC-I feedback loop.

We advance the tentative conclusion that the partial RC peak migrated westward during 1400 to 1645 UT. This conclusion is not inconsistent with elementary drift physics. Suppose that at 1400 UT, the partial RC peak was at 2200 MLT and comprised ions of 5–20 keV. We assume a dipole field to provide an upper limit on the drift time. At $L = 4$, these ions would require 1 h to 3 h to reach 2000 MLT. Actual drift times in a nondipolar field (e.g., during 1400–1700 UT the mean *Dst* was ∼ −95 nT) would be shorter than this estimate. Some caution is warranted in advancing this interpretation, which is based upon a comparison of absolute flux measurements from two different satellites (cf. cross-calibration discussion above).

5.6. Isolated Midstorm Injection

In this section we use Van Allen Probes and TWINS observations to study an isolated injection event that occurred during the 17 March 2015 storm. The term "isolated" refers to the fact that the injection is temporally distinct: a sharp increase that occurred during a temporary abatement in ring current flux.

Figures 10a–10c provide equatorial snapshots of the models (PTP and magnetosheath), Van Allen Probes orbits, and TWINS global maps of ion flux from the nearest-in-time ENA image. In each equatorial plot, the

locations of RBSP A and B are plotted (as dots) at the time indicated at the top of the plot. The TWINS ion map is from the time stamp shown in the colorbar in the bottom right corner. Beneath each equatorial plot are spectra (flux versus energy) of RBSP A protons and TWINS 1 ions, at the corresponding locations shown in the orbit plot. Note the color-coded flux scales (ordinate axis of plot) for RBSP and TWINS. Figures 10d and 10e are RBSP A and RBSP B proton flux spectrograms, plotted between 1700 UT and 1930 UT.

5.6.1. Flux During the Injection (RBSP and TWINS)

Between 1715 UT (Figure 10a) and 1745 UT (Figure 10b), the TWINS equatorial ion flux more than doubled. The global maximum of the RC crescent rose from 340 $(cm^2\,sr\,s\,eV)^{-1}$ at 1715 UT ($L = 3.7$, 1957 MLT) to 780 $(cm^2\,sr\,s\,eV)^{-1}$ at 1745 UT ($L = 3.6$, 1946 MLT). RBSP A, at the outer edge of the global crescent of the partial RC, likewise saw a doubling of its peak flux, from $\sim 2 \times 10^4$ $(cm^2\,sr\,s\,eV)^{-1}$ at 1710 UT (Figure 10a, spectrum) to $\sim 4 \times 10^4$ $(cm^2\,sr\,s\,eV)^{-1}$ at 1740 UT (Figure 10b). Because this flux doubling occurred against a backdrop of otherwise abated activity (compared to several hours earlier in the storm), this injection appears comparatively isolated in the spectrogram of Figure 10d. During this time, RBSP B saw only background counts (Figure 10e) and apparently missed the injection.

The fact that the local and global spectral shapes of Figure 10 do not agree deserves consideration. The TWINS spectra have two distinct peaks (5 keV and ~30 keV), whereas the RBSP A spectra each contain a broad ~9 keV peak. (The 1740 UT spectrum also has a 1 keV peak.) Note that both TWINS and Van Allen Probes had observed a double-peak spectrum very close to the RC global maximum, a short while earlier (Figure 9c, spectrum plot). We can reconcile these observations if there was significant spatial variation of the ion spectra. Specifically, we propose that the double-peak spectrum occurred in the center of the RC crescent, but the spectral properties varied across the outer flux gradient (see location of RBSP A in equatorial plot of Figure 10b). The local measurements by RBSP A would reflect this fine-scale structure. The TWINS measurements, having much coarser spatial resolution (as explained earlier in section 5.5.3), might not. In fact, we speculate that the TWINS inversion, a mathematical solution to the underconstrained problem of extracting ion distributions from ENA images, is possibly influenced by the energy spectrum of the peak. Indeed, the TWINS spectrum in Figure 10c, sampled well outside the main crescent, still exhibits a double-peak spectral dependence. Another aspect of the observations that we do not herein consider is pitch angle distribution. The TWINS global observations at this time indicate a PAD that is more pancake than isotropic [*Perez et al.*, 2016], which might influence the flux of energetic neutrals reaching an imager viewing from above the SM equatorial plane.

About 1.5 h after the injection (Figure 10c), the TWINS ion flux had ebbed to nearly its preinjection level: the global flux maximum dropped to 400 $(cm^2\,sr\,s\,eV)^{-1}$ at 1859 UT. At 1910 UT (Figure 10c) RBSP A observed a less energetic spectrum as the spacecraft moved completely outside the RC cresent (see equatorial plot), again suggestive of a spatial dependence to the ion spectral properties.

5.6.2. Energetics of Precipitating Ions

We next explore further the dynamics and energetics of the 1740 UT injection, using TWINS global imaging data.

Figures 11a–11c contain TWINS 1 ENA images (16 keV) from before, during, and after the injection. In each image, the Earth is the sphere (with the latitude and longitude grid) in the top left, and dipole field lines are drawn at $L = (4, 8)$ and (06, 12, 18, 24) MLT. RBSP (A and B) orbits and instantaneous locations are overplotted.

The injection is clear in the sequence of ENA images as a doubling of flux in the premidnight sector, i.e., the bottom right corner region between the gray field lines (labeled "1800") and the white field lines ("2400"). Before the injection (Figure 11a) average premidnight flux was ~ 0.1 $(cm^2\,sr\,s\,eV)^{-1}$ (yellow-green). During the injection (Figure 11b) the average premidnight flux was ~0.2 $(cm^2\,sr\,s\,eV)^{-1}$ (orange-red). By 1859 UT (Figure 11c) the 16 keV flux had decreased again.

Figures 11d–11f contain energy-versus-MLT spectrograms of low-altitude, precipitating ion flux. These fluxes are derived from the so-called low-altitude emission (LAE), the intense ENA signal from near the Earth limb [*Brandt et al.*, 2001; *Bazell et al.*, 2010]. The LAE signal is labeled in each of the ENA images of Figure 11. LAE flux is converted to ion flux using the method of *Goldstein et al.* [2016]. It must be noted that because of highly anisotropic pitch angle distributions at low altitudes, the LAE signal is highly directional and thus viewing geometry dependent. LAEs are typically visible only within a crescent-shaped region localized to the limb opposite an ENA imager [*Bazell et al.*, 2010]; outside of this crescent low-altitude ENA fluxes are attenuated and thus cannot be reliably converted to ion flux. This effect is apparent in the ENA images. For example, in Figure 11a TWINS 1 was located near dusk so it could only see LAEs within a few MLT hours of dawn.
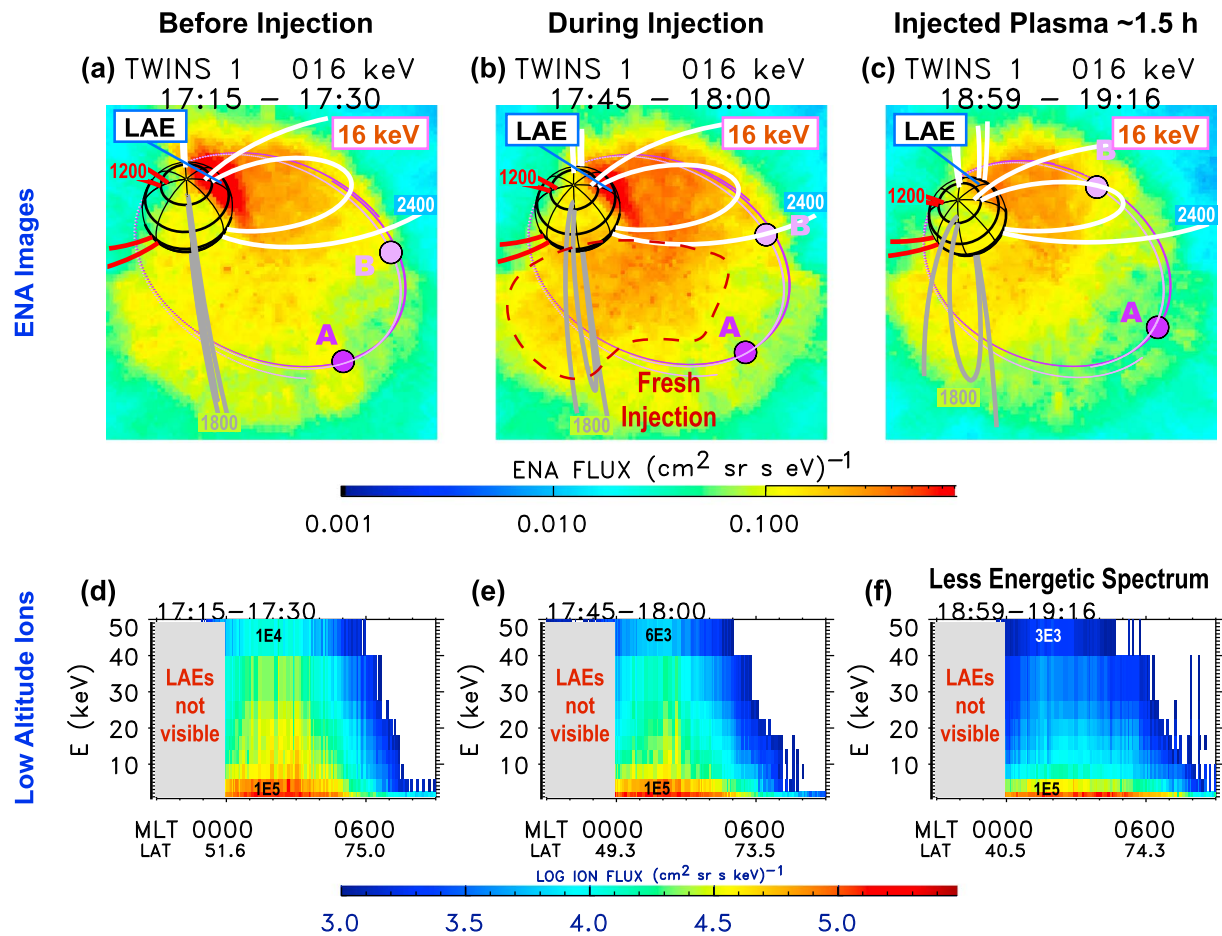
Figure 11. TWINS global (contextual) observations before, during, and after 1740 UT injection. (a–c) TWINS 1 ENA images with RBSP orbits overplotted (lavender). (d–f) TWINS 1 precipitating (low-altitude) ion spectrograms (flux versus energy, MLT).

This limitation means that even if there was extremely intense precipitation near dusk, TWINS would measure only a weak (attenuated) signal there. Accordingly, the region west of 0000 MLT is annotated as "LAEs not visible" in the energy-versus-MLT spectrograms. On the other hand, 0600 MLT is well within the visibility crescent, yet there is a steep drop in flux east of the dawn terminator (Figure 11d). Therefore, this dawnside dropoff reflects an actual gradient in precipitating ion flux rather than a viewing geometry effect.

At all times there was moderate-to-strong precipitation in the postmidnight (0000–0600 MLT) sector, although as noted directly above, there could have been premidnight precipitation as well, which would not be visible to TWINS. Before the injection (Figure 11d) low-altitude ion flux exhibited a falling spectrum, from $\sim 1 \times 10^5 \left(cm^2\, sr\, s\, eV \right)^{-1}$ at 1 keV to about $\sim 1 \times 10^4 \left(cm^2\, sr\, s\, eV \right)^{-1}$ at 50 keV. During the injection (Figure 11e) the flux spectra softened, e.g., with 50 keV flux falling by 40% across 6 h of local time. About 1.5 h after the injection (Figure 11d) there was a decrease in precipitating ion flux at all energies >1 keV; e.g., the average postmidnight 50 keV flux dropped to $\sim 3 \times 10^3 \left(cm^2\, sr\, s\, eV \right)^{-1}$, approximately 30% of its preinjection level. The net result: after the injection, the TWINS-measured precipitating ions were globally less energetic (softer).

However, it must be noted that between 1745 UT (Figure 11b) and 1859 UT (Figure 11c) TWINS 1 moved along its orbit, introducing possible viewing-geometry effects to the LAE intensity [*Goldstein et al.*, 2016]. During this interval the spacecraft moved 0.6 R_E in radius (from 6.4 R_E to 7.0 R_E), 1 h in local time (1800 to 1900 MLT) and 5° in latitude (60° to 65°). The changes in latitude and MLT are especially important for measuring the highly directional LAE signal because they can (more strongly than radius) affect the range of latitudes at which an LAE is sampled [*Goldstein et al.*, 2016]. In each energy-MLT spectrogram of Figure 11 the abcissa is also labeled by its magnetic latitude values; note that each of these values denotes the latitude of the center of the LAE source location (not the imager location). To judge the effect of the viewing geometry change
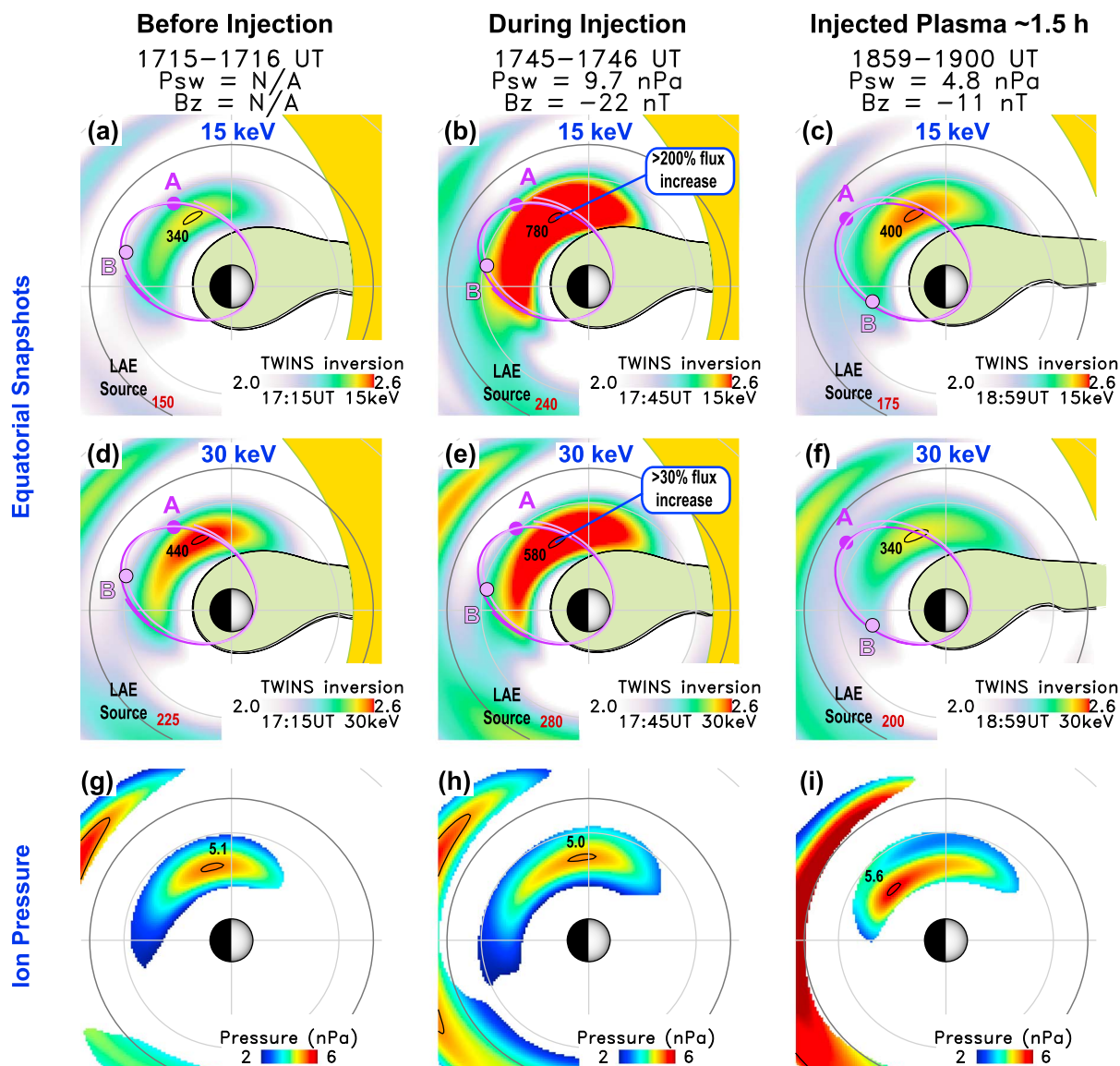
Figure 12. TWINS 1 global ion flux and pressure before, during, and after 1740 UT injection. (a and c) Global TWINS 1 (15 keV) ion flux. (d–f) Global TWINS 1 (30 keV) ion flux. (g–i) TWINS 1 total ion pressure.

between Figures 11and 11f, we compare the change in source (LAE) latitude at two MLT tick marks spanning the emission: at 0000 MLT (0600 MLT) the source latitude changed 9° (0.8°). Thus, the latitudinal viewing geometry change was stronger for LAE observations near midnight than near dawn. If the viewing geometry change was responsible for the spectral softening effect, the spectrum should be softer (less energetic) near midnight than at dawn; instead, the opposite is true.

5.6.3. Energetics of Trapped Ions

To investigate whether this evolution toward less energetic spectra also occurred in the trapped/high-altitude ring current ions, Figure 12 shows equatorial ion maps at two energies (15 and 30 keV) and total ion pressure. All the flux plots share the same colorbar. The ion pressure maps are filtered to remove regions for which ion flux (at 30 keV) is below 210 $(cm^2 \, sr \, s \, eV)^{-1}$, i.e., 50% of the upper limit of the flux colorbar.

Before the injection 30 keV flux was higher than at 15 keV (Figures 12a and 12d). At 1715 UT the 30 keV ring current crescent had a maximum of 440 $(cm^2 \, sr \, s \, eV)^{-1}$ at ($L = 3.6$, 1938 MLT), 30% larger than the 15 keV peak of 340 $(cm^2 \, sr \, s \, eV)^{-1}$ at ($L = 3.7$, 1957 MLT). The 1740 UT injection changed this ratio by bringing in new ions with a less energetic spectrum (Figures 12b and 12e). At 1745 UT the 15 keV flux had more than doubled,

to 780 $\left(\text{cm}^2\,\text{sr}\,\text{s}\,\text{eV}\right)^{-1}$, while the 30 keV flux increased by only 30% to 580 $\left(\text{cm}^2\,\text{sr}\,\text{s}\,\text{eV}\right)^{-1}$. After the injection, a less energetic spectral ratio persisted (Figures 12c and 12f), with 30 keV flux at 85% of that at 15 keV.

Taken at face value, this observation suggests that individual injections may either raise or lower the average energy at a given location, depending on how hot the fresh ions are compared to the older ion population. This may help explain observed intervals of reduced global ion temperature during the main phase of CME-driven storms [*Keesee et al.*, 2014b]. However, this interpretation must not be overstated. Two-point energy sampling (at 15 and 30 keV, as in Figure 12) of the flux spectrum offers a limited view of complicated storm time ion energetics. As noted earlier, the TWINS inversion data contain nonmonotonic, multipeak spectra inside the RC crescent (Figure 10). Moreover, Van Allen Probes in situ data indicate that ion flux spectra both vary in space and evolve with time. For example, RBSP A recorded time-dependent flux spectra distinct from those remotely sensed by TWINS in the center of the RC crescent, ∼1 R_E removed from RBSP A's location (Figure 12b).

Such changes in flux at particular energies, or at specific locations and times, occur against a larger backdrop of systemic evolution of the storm. Individual injections may bring in cooler or warmer plasma, but during the main phase the overall trend is a pressure increase, as illustrated in Figure 12 (bottom row). Even as flux rose or fell depending on energy (Figures 12a through 12f), the pressure increased (Figures 12g through 12i). Before the injection, the peak pressure inside geosynchronous orbit was ∼5 nPa; afterward, it was ∼6 nPa.

As shown in Figures 12a through 12f, during this interval the global flux peak $\left(> 300\,\left(\text{cm}^2\,\text{sr}\,\text{s}\,\text{eV}\right)^{-1}\right)$ of the trapped ring current ions was in the premidnight sector at $L < 4$. In the postmidnight sector, at $L \approx 6.6$ (geosynchronous orbit), there was a second region of weaker ion flux ($< 300\,(\text{cm}^2\,\text{sr}\,\text{s}\,\text{eV})^{-1}$). This weaker-flux region (labeled "LAE Source," with per-region flux maximum labeled in red) is the source of the precipitating ions in the postmidnight sector, shown earlier in Figure 12. Because the source of TWINS-observed ion precipitation was at or outside geosynchronous orbit, it may be argued that the precipitating ions came from the plasma sheet rather than the ring current. According to the TWINS inversions, this high-L LAE source region — the reservoir for the ion precipitation — was a region of high ion pressure as well, as shown in Figures 12g through 12i. Elevated plasma sheet pressure during an injection is consistent with AMPTE CCE data analysis by *Kistler et al.* [1992], who found that substorm injections may increase the plasma sheet ion pressure to several nanopascals for $L < 8$.

6. Discussion

6.1. Ring Current Response

Geomagnetic storms are largely defined by the ring current response, two fundamental measures of which are flux and energy. The difference between the quiet time and storm time ring current is profound. In the early hours of 17 March 2015, before the storm began, protons drifted in a stable, quiescent zone (above $L \approx 4$) of double-nose flux-versus-energy spectra. The double-nose structure on 17 March was stable enough that the two Van Allen Probes observed nearly identical spectral peaks at the same location (L, MLT) but 6 UT hours apart. In contrast, the storm time observations depict an extremely dynamic energetic ion environment, both varying in space and evolving in time, often with rapid, seemingly chaotic changes in flux intensity and energy.

To quantify these dynamics, the flux peak above 1 keV was automatically extracted from RBSP A and RBSP B (HOPE) spectrograms, at 30 s cadence, for the entire day. The result is shown in Figure 13, which provides a synoptic view of the RC response on 17 March 2015, as measured by the two Van Allen Probes. Figure 13a plots the flux at the peak, and Figure 13b plots the energy. Figure 13c shows B_z.

About 10–15 min after the 0605 UT southward IMF turning, as the CCB was convected past the spacecraft (section 4), RBSP B recorded a steep flux increase (Figure 13a) with an E^{-2} flux dependence; i.e., as the peak flux increased, the energy of the peak plummeted (Figure 13b). Roughly 1 h later, as RBSP A emerged from the plasmasphere, it also saw a steep (in this case E^{-3}) flux increase. Because both these dramatic flux increases occurred at or near a cold plasma boundary, we conclude that early in the storm the cold plasma plays an important role in demarcating the newly injected ring current, because the cold plasma and ring current particles are influenced by the same convection field and form boundaries at a similar location. During the ∼0700–1200 UT interval of structured, dynamic ion signatures (numerous injections and multiple spectral peaks both broad and narrow), the peak flux (Figure 13a) fluctuated considerably, and the peak energy (Figure 13b) exhibited major excursions spanning two decades.
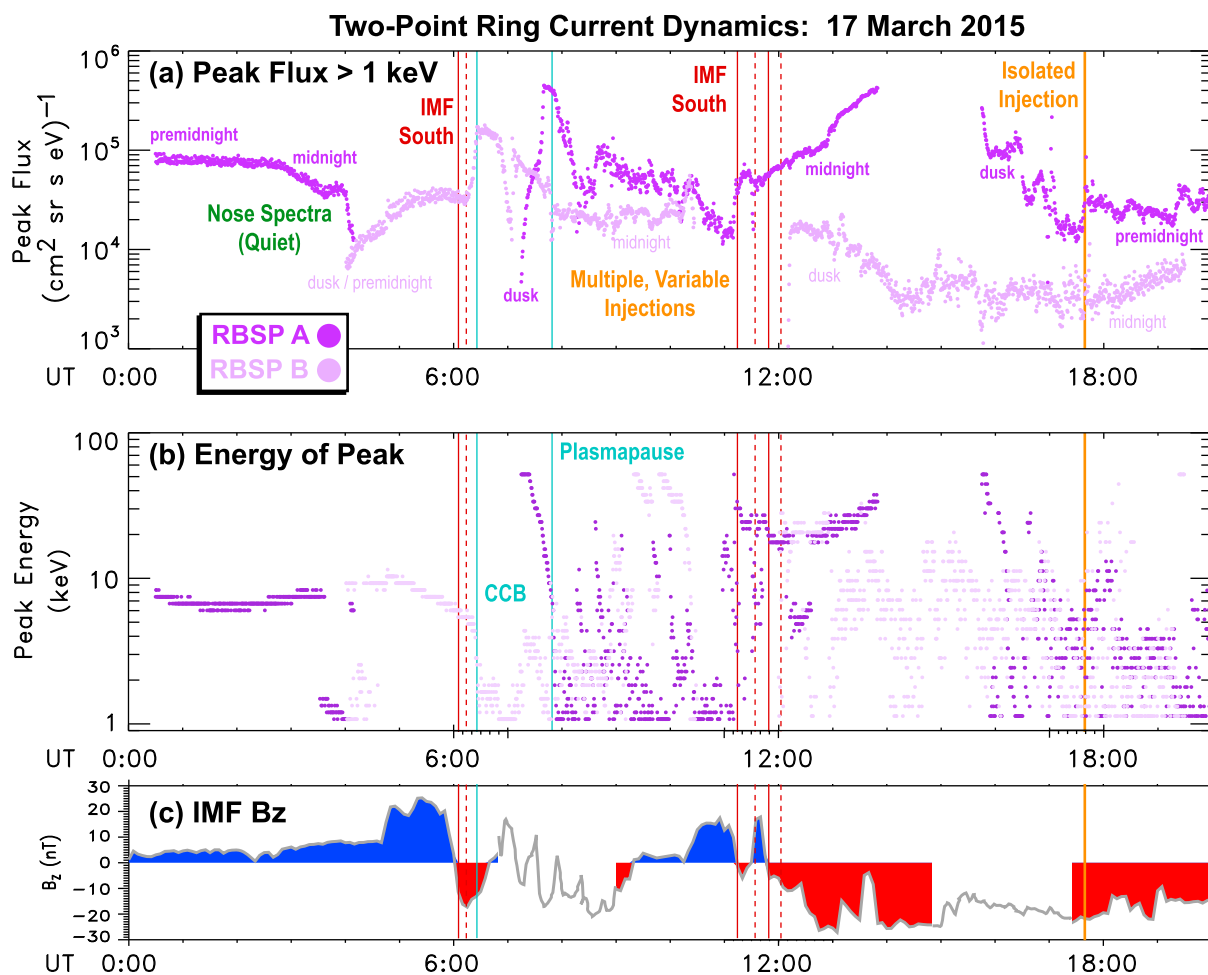
Figure 13. Summary of 17 March 2015 ring current response as measured by the two Van Allen Probes. (a and b) Peak flux value and energy above 1 keV, automatically extracted at 30 s cadence. (c) IMF B_Z.

The in situ observations presented in this paper indicate highly structured convective flows and fields. The global process of plasma injection apparently comprises a large number of individual, bursty ion structures, as numerous raindrops and gusts of wind collectively make a rainstorm. Images allow us to see the partial ring current intensify, expand, and migrate [e.g., *Brandt et al.*, 2005; *Goldstein et al.*, 2005b] but can capture only the coarser attributes of the bursty, structured process (e.g., multiple spatial and/or spectral peaks). At the same time, global RC peaks both evolve and migrate during storms, making it difficult to interpret in situ data without global context.

6.2. Cross-Scale Magnetospheric Response

This study builds upon previous multimission results that have used TWINS images together with data from THEMIS, Van Allen Probes, or IBEX. *Fok et al.* [2010] compared TWINS and THEMIS data with a global ring current model to demonstrate the importance of self-consistent magnetic fields. *Perez et al.* [2012] compared TWINS and THEMIS flux spectra, finding non-Maxwellian distributions and obtaining reasonably good global-to-local agreement in absolute flux. *Grimes et al.* [2013] used THEMIS data to validate TWINS-derived global flux and pitch angle distributions, finding higher pitch angle anisotropy at lower *L* values. *Keesee et al.* [2014a] found good agreement between the spectral shapes of TWINS and THEMIS measurements, both showing non-Maxwellian distributions. *Perez et al.* [2015] obtained good agreement (in absolute flux) between THEMIS and TWINS measurements and demonstrated the presence of multiple spatial and spectral peaks in the ring current. *Fok et al.* [2014] used TWINS and Van Allen Probes data along with their global ring current model to demonstrate the importance of self-consistent electric fields and found that adiabatic acceleration and drift losses were dominant during a CME driven storm. *Valek et al.* [2015] obtained good agreement (in absolute flux) between multispecies (hydrogen and oxygen) TWINS and Van Allen Probes measurements

and determined that globally enhanced regions of ion flux comprise multiple smaller-spatial-scale ion structures. In all of this previous work involving TWINS and other mission data sets, emphasis has been placed on validation of the global imaging results or improvement of global models. Our three-way comparison of flux spectra from Van Allen Probes, THEMIS, and TWINS (Figure 9c) adds to this collection of research. We find some disagreement in absolute flux, not just between the imaging and in situ data but between the two different in situ measurements as well. This disparity in local fluxes suggests that while validation of ENA-derived fluxes is valuable, the community's view of "ground truth" data may require some revision. Consistent with previous results, we find evidence — in the combined three-mission data set — of multiple spectral peaks and significant spatial structure in the storm time ring current.

Beyond validation studies, the combined use of multiple mission data sets enables tracking dynamic linkages among different processes and regions of the magnetosphere. *McComas et al.* [2012] used global IBEX images of the dayside magnetospheric boundary together with TWINS images to study the timing and energetics of the ring current response to a global, dayside compression event. Complementing and extending this previous work, our study uses three missions together to track the progress of the 17 March 2015 event, from its inception at the dayside magnetospheric boundary to the inner magnetosphere during the main phase of the storm. The dayside boundary dynamics were captured by the multipoint local measurements of THEMIS, interpreted with the aid of simple models for the bow shock and magnetopause [*Shue et al.*, 1997; *Jelínek et al.*, 2012]. We validated these boundary models by direct comparison with the THEMIS data. In the inner magnetosphere, Van Allen Probes observations of the onset of convection were similarly interpreted via a simple model for the plasmapause [*Goldstein et al.*, 2014b]. We also validated this model by direct comparison with Van Allen Probes data. The two-point Van Allen Probes measurements reveal both quiescent nose-like structures before the storm hit and the variety of spatial, spectral, and temporal structures once the storm commenced. The TWINS images provide insight into how these local structures evolve into or contribute to global regions of enhanced ring current pressure and how individual injection events can affect both spatial distributions and spectra.

6.3. Why Simple Models?

In this study we have demonstrated how cross-scale measurements, combined with contextual models, can provide a more complete picture of the storm than any one source of information. The models used in this study [*Shue et al.*, 1997; *Jelínek et al.*, 2012; *Goldstein et al.*, 2014b] have one major practical advantage: they are computationally inexpensive and thus very easy to use routinely (e.g., automatically) on a large data set. More sophisticated models offer great insight into physical processes but with this benefit comes more computational cost and complexity. Given the availability of repositories of multiple years of PTP simulations (via the ECT link at http://rbspgway.jhuapl.edu/) and the ease of computing empirical bow shock and magnetopause locations, it becomes possible to apply our cross-scale, data-model methodology to multiple storm events. This work can be pursued in future studies.

7. Summary

We conclude by briefly summarizing our results. This paper presents cross-scale magnetospheric observations of the 17 March 2015 (St. Patrick's Day) storm, by THEMIS, the Van Allen Probes (RBSP), and TWINS. To gauge the energy input to the system, we use upstream solar wind data from ACE/Wind.

On 17 March, THEMIS crossed the bow shock or magnetopause 22 times. Included in these boundary crossings are THEMIS observations of the dayside magnetospheric compression that initiated the storm. Empirical models [*Jelínek et al.*, 2012; *Shue et al.*, 1997] reproduce the observed boundary locations with an average error of 0.7 R_E. Van Allen Probes crossed the plasmapause 13 times and a test particle simulation [*Goldstein et al.*, 2014b] reproduces these encounters with an average error of 0.5 R_E.

Before the storm, Van Allen Probes measured quiet double-nose proton spectra in the region of corotating, partially depleted cold plasma. About 15 min after a 0605 UT dayside southward turning, RBSP B captured the onset of inner magnetospheric convection, in the form of (1) a density decrease at the moving corotation-convection boundary (CCB) and (2) a steep increase in ring current (RC) proton flux. During the first several hours of the storm, Van Allen Probes measured highly dynamic ion signatures (numerous injections and multiple spectral peaks both broad and narrow). Sustained convection after ~1200 UT initiated a major buildup of the midnight-sector ring current (measured by RBSP A), with much weaker duskside fluxes (measured by

RBSP B, THEMIS a, and THEMIS d). A close conjunction of THEMIS d, RBSP A, and TWINS 1 at 1631 UT shows good three-way agreement in the shapes (but not the absolute fluxes) of two-peak spectra from the center of the partial RC. A midstorm injection, observed by Van Allen Probes and TWINS at 1740 UT, brought in fresh ions with lower average energies (leading to globally cooler spectra in precipitating ions) but increased the total pressure.

The cross-scale measurements (interpreted with the help of models) contain a great deal of spatial, spectral, and temporal structure, suggesting that storm time plasma transport comprises a large number of individual, bursty flows, and ion structures. Multimission measurements, combined with simple models, can provide a more complete picture of the storm than any one source of information.

References

Angelopoulos, V. (2008), The THEMIS mission, *Space Sci. Rev.*, *141*, 5–34, doi:10.1007/s11214-008-9336-1.

Angelopoulos, V., and et al. (2008), First results from the THEMIS mission, *Space Sci. Rev.*, *141*, 453–476, doi:10.1007/s11214-008-9378-4.

Bazell, D., E. Roelof, T. Sotirelis, P. Brandt, H. Nair, P. Valek, J. Goldstein, and D. McComas (2010), Comparison of TWINS images of low-altitude emission (LAE) of energetic neutral atoms with DMSP precipitating ion fluxes, *J. Geophys. Res.*, *115*, A10204, doi:10.1029/2010JA015644.

Brandt, P. C., S. Barabash, E. C. Roelof, and C. J. Chase (2001), Energetic neutral atom imaging at low altitudes from the Swedish microsatellite Astrid: Observations at low (≤10 keV) energies, *J. Geophys. Res.*, *106*, 24663, doi:10.1029/2000JA900119.

Brandt, P. C., P. S. Ohtani, D. G. Mitchell, M.-C. Fok, E. C. Roelof, and R. DeMajistre (2002), Global ENA observations of the storm mainphase ring current: Implications for skewed electric fields in the inner magnetosphere, *Geophys. Res. Lett.*, *29*(20), 1954, doi:10.1029/2002GL015160.

Brandt, P. C., J. Goldstein, P. C. Anderson, R. DeMajistre, E. C. Roelof, and D. G. Mitchell (2005), On the relation between sub-auroral electric fields, the ring current and the plasmasphere, in *The Inner Magnetosphere: Physics and Modeling*, edited by T. I. Pulkkinen, N. A. Tsyganenko, and R. H. W. Friedel, pp. 163, AGU, Washington, D. C.

Burch, J. L. (2005), Magnetospheric imaging: Promise to reality, *Rev. Geophys.*, *43*, RG3001, doi:10.1029/2004RG000160.

Burke, W. J., P. J. Erickson, J. Yang, J. Foster, J. Wygant, G. Reeves, and C. Kletzing (2016), O^+ ion conic and plasma sheet dynamics observed by Van Allen Probe satellites during the 1 June 2013 magnetic storm, *J. Geophys. Res. Space Physics*, *121*, 4072–4091, doi:10.1002/2015JA021795.

Buzulukova, N. Y., Y. I. Galperin, R. A. Kovrazhkin, A. L. Glazunov, G. A. Vladimirova, H. Stenuit, J. A. Sauvaud, and D. C. Delcourt (2002), Two types of ion spectral gaps in the quiet inner magnetosphere: Interball-2 observations and modeling, *Ann. Geophys.*, *20*, 349–364, doi:10.5194/angeo-20-349-2002.

Buzulukova, N. Y., R. A. Kovrazhkin, A. L. Glazunov, J.-A. Sauvaud, N. Y. Ganushkina, and T. I. Pulkkinen (2003), Stationary nose structures of protons in the inner magnetosphere: Observations by the ION instrument onboard the Interball-2 satellite and modeling, *Cosmic Res.*, *41*, 3–12.

Coroniti, F. V., and C. F. Kennel (1973), Can the ionosphere regulate magnetospheric convection?, *J. Geophys. Res.*, *78*, 2837–2851, doi:10.1029/JA078i016p02837.

Ejiri, M., R. A. Hoffman, and P. H. Smith (1980), Energetic particle penetrations into the inner magnetosphere, *J. Geophys. Res.*, *85*, 653–663, doi:10.1029/JA085iA02p00653.

Ferradas, C., J. Zhang, H. Luo, L. M. Kistler, H. E. Spence, B. Larsen, R. M. Skoug, H. O. Funsten, and G. D. Reeves (2014), *Ion spectral structures observed by the Van Allen Probes and Cluster*, Abstract SM43A-4253 presented at 2014 Fall Meeting Abstracts, AGU, San Francisco, Calif., 15–19 Dec.

Ferradas, C. P., J.-C. Zhang, H. E. Spence, L. M. Kistler, B. A. Larsen, G. Reeves, R. Skoug, and H. Funsten (2016), Drift paths of ions composing multiple-nose spectral structures near the inner edge of the plasma sheet, *Geophys. Res. Lett.*, *43*, 11,484–11,492, doi:10.1002/2016GL071359.

Ferradas, C. P., J.-C. Zhang, L. M. Kistler, and H. E. Spence (2015), Heavy-ion dominance near Cluster perigees, *J. Geophys. Res.*, *120*(12), 10,485–10,505, doi:10.1002/2015JA021063.

Fok, M.-C., J. U. Kozyra, A. F. Nagy, and T. E. Cravens (1991), Lifetime of ring current particles due to Coulomb collisions in the plasmasphere, *J. Geophys. Res.*, *96*, 7861–7867, doi:10.1029/90JA02620.

Fok, M.-C., J. U. Kozyra, A. F. Nagy, C. E. Rasmussen, and G. V. Khazanov (1993), Decay of equatorial ring current ions and associated aeronomical consequences, *J. Geophys. Res.*, *98*, 19381–19393, doi:10.1029/93JA01848.

Fok, M.-C., N. Buzulukova, S.-H. Chen, P. W. Valek, J. Goldstein, and D. J. McComas (2010), Simulation and TWINS observations of the 22 July 2009 storm, *J. Geophys. Res.*, *115*, A12231, doi:10.1029/2010JA015443.

Fok, M.-C., N. Y. Buzulukova, S.-H. Chen, A. Glocer, T. Nagai, P. Valek, and J. D. Perez (2014), The comprehensive inner magnetosphere-ionosphere model, *J. Geophys. Res. Space Physics*, *119*, 7522–7540, doi:10.1002/2014JA020239.

Fok, M.-C., et al. (2003), Global ENA IMAGE simulations, *Space Sci. Rev.*, *109*, 77–103.

Funsten, H. O., et al. (2013), Helium, oxygen, proton, and electron (HOPE) mass spectrometer for the Radiation Belt Storm Probes mission, *Space Sci. Rev.*, *179*, 423–484, doi:10.1007/s11214-013-9968-7.

Goldstein, J., and D. J. McComas (2013), Five years of stereo magnetospheric imaging by TWINS, *Space Sci. Rev.*, *180*(1–4), 39–70, doi:10.1007/s11214-013-0012-8.

Goldstein, J., and B. R. Sandel (2005), The global pattern of evolution of plasmaspheric drainage plumes, in *Inner Magnetosphere Interactions: New Perspectives from Imaging*, edited by J. L. Burch, M. Schulz, and H. Spence, p. 1, AGU, Washington, D. C., doi:10.1029/159GM01.

Goldstein, J., B. R. Sandel, W. T. Forrester, and P. H. Reiff (2003), IMF-driven plasmasphere erosion of 10 July 2000, *Geophys. Res. Lett.*, *30*(3), doi:10.1029/2002GL016478.

Goldstein, J., J. L. Burch, and B. R. Sandel (2005a), Magnetospheric model of subauroral polarization stream, *J. Geophys. Res.*, *110*, A09222, doi:10.1029/2005JA011135.

Goldstein, J., J. L. Burch, B. R. Sandel, S. B. Mende, P. C. Brandt, and M. R. Hairston (2005b), Coupled response of the inner magnetosphere and ionosphere on 17 April 2002, *J. Geophys. Res.*, *110*, A03205, doi:10.1029/2004JA010712.

Goldstein, J., B. R. Sandel, M. F. Forrester, T. F. Thomsen, and M. R. Hairston (2005c), Global plasmasphere evolution 22–23 April 2001, *J. Geophys. Res.*, *110*, A12218, doi:10.1029/2005JA011282.

Goldstein, J., M. F. Thomsen, and A. DeJong (2014a), In situ signatures of residual plasmaspheric plumes, *J. Geophys. Res. Space Physics*, *119*, 4706–4722, doi:10.1002/2014JA019953.

Goldstein, J., D. V. Bisikalo, V. I. Shematovich, J.-C. Gérard, F. Søraas, D. J. McComas, P. W. Valek, K. LLera, and J. Redfern (2016), Analytical estimate for low-altitude ENA emissivity, *J. Geophys. Res. Space Physics*, *121*, 1167–1191, doi:10.1002/2015JA021773.

Goldstein, J., et al. (2014b), Simulation of Van Allen Probes plasmapause encounters, *J. Geophys. Res. Space Physics*, *119*, 7464–7484, doi:10.1002/2014JA020252.

Grimes, E. W., J. D. Perez, J. Goldstein, D. J. McComas, P. Valek, and D. Turner (2013), Comparison of TWINS and THEMIS observations of proton pitch angle distributions in the ring current during the 29 May 2010 geomagnetic storm, *J. Geophys. Res. Space Physics*, *118*(8), 4895–4905, doi:10.1002/jgra.50455.

Jelínek, K., Z. Němeček, and J. Šafránková (2012), A new approach to magnetopause and bow shock modeling based on automated region identification, *J. Geophys. Res.*, *117*, A05208, doi:10.1029/2011JA017252.

Kanekal, S. G., et al. (2016), Prompt acceleration of magnetospheric electrons to ultrarelativistic energies by the 17 March 2015 interplanetary shock, *J. Geophys. Res. Space Physics*, *121*, 7622–7635, doi:10.1002/2016JA022596.

Keesee, A. M., M. W. Chen, E. E. Scime, and A. T. Y. Lui (2014a), Regions of ion energization observed during the Galaxy-15 substorm with TWINS, *J. Geophys. Res. Space Physics*, *119*(10), 8274–8287, doi:10.1002/2014JA020466.

Keesee, A. M., J. G. Elfritz, M.-C. Fok, D. McComas, and E. Scime (2014b), Superposed epoch analysis of ion temperature evolution during CME- and CIR/HSS-driven storms, *J. Atmos. Sol. Terr. Phys.*, *115*, 67–78, doi:10.1016/j.jastp.2013.08.009.

Kistler, L. M., E. Möbius, W. Baumjohann, G. Paschmann, and D. C. Hamilton (1992), Pressure changes in the plasma sheet during substorm injections, *J. Geophys. Res.*, *97*, A03209, doi:10.1029/91JA02802.

Kivelson, M. G., and C. T. Russell (1995), *Introduction to Space Physics*, Cambridge Univ. Press, New York.

Kletzing, C. A., et al. (2013), The electric and magnetic field instrument suite and integrated science (EMFISIS) on RBSP, *Space Sci. Rev.*, *179*, 127–181, doi:10.1007/s11214-013-9993-6.

Kurth, W. S., S. De Pascuale, J. B. Faden, C. A. Kletzing, G. B. Hospodarsky, S. Thaller, and J. R. Wygant (2015), Electron densities inferred from plasma wave spectra obtained by the Waves instrument on Van Allen Probes, *J. Geophys. Res. Space Physics*, *120*, 904–914, doi:10.1002/2014JA020857.

Lepping, R. P., et al. (1995), The WIND magnetic field investigation, *Space Sci. Rev.*, *71*, 207–229.

Mauk, B. H., N. J. Fox, S. G. Kanekal, R. L. Kessel, D. G. Sibeck, and A. Ukhorskiy (2013), Science objectives and rationale for the radiation belt storm probes mission, *Space Sci. Rev.*, *179*, 3–27, doi:10.1007/s11214-012-9908-y.

NASA Heliophysics Roadmap (2014), *Our Dynamic Space Environment: Heliophysics Science and Technology Roadmap for 2014–2033*, NASA Headquarters, Washington, D. C.

McComas, D. J., N. Buzulukova, M. G. Connors, M. A. Dayeh, J. Goldstein, H. O. Funsten, S. Fuselier, N. A. Schwadron, and P. Valek (2012), Two Wide-Angle Imaging Neutral-Atom Spectrometers and Interstellar Boundary Explorer energetic neutral atom imaging of the 5 April 2010 substorm, *J. Geophys. Res.*, *117*, A03225, doi:10.1029/2011JA017293.

McComas, D. J., et al. (2009), The two wide-angle imaging neutral-atom spectrometers (TWINS) NASA mission-of-opportunity, *Space Sci. Rev.*, *142*(1–4), 157–231, doi:10.1007/s11214-008-9467-4.

McFadden, J. P., C. W. Carlson, D. Larson, M. Ludlam, R. Abiad, B. Elliott, P. Turin, M. Marckwordt, and V. Angelopoulos (2008), The THEMIS ESA plasma instrument and in-flight calibration, *Space Sci. Rev.*, *141*(1–4), 277–302, doi:10.1007/s11214-008-9440-2.

O'Brien, T. P., and M. B. Moldwin (2003), Empirical plasmapause models from magnetic indices, *Geophys. Res. Lett.*, *30*(4), 1152, doi:10.1029/2002GL016007.

Ogilvie, K. W., et al. (1995), SWE, a comprehensive plasma instrument for the wind spacecraft, *Space Sci. Rev.*, *71*, 55–77.

Perez, J. D., E. W. Grimes, J. Goldstein, D. J. McComas, P. Valek, and N. Billor (2012), Evolution of CIR storm on 22 July 2009, *J. Geophys. Res.*, *117*, A09221, doi:10.1029/2012JA017572.

Perez, J. D., J. Goldstein, D. J. McComas, P. Valek, N. Buzulukova, M.-C. Fok, and H. J. Singer (2015), TWINS stereoscopic imaging of multiple peaks in the ring current, *J. Geophys. Res. Space Physics*, *120*, 368–383, doi:10.1002/2014JA020662.

Perez, J. D., J. Goldstein, D. J. McComas, P. Valek, M. Fok, and K.-J. Hwang (2016), Global images of trapped ring current ions during main phase of 17 March 2015 geomagnetic storm as observed by TWINS, *J. Geophys. Res. Space Physics*, *121*, 6509–6525, doi:10.1002/2016JA022375.

Shue, J.-H., J. K. Chao, H. C. Fu, C. T. Russell, P. Song, K. K. Khurana, and H. J. Singer (1997), A new functional form to study the solar wind control of the magnetopause size and shape, *J. Geophys. Res.*, *102*, 9497–9511, doi:10.1029/97JA00196.

Smith, P. H., and R. A. Hoffman (1974), Direct observations in the dusk hours of the characteristics of the storm time ring current particles during the beginning of magnetic storms, *J. Geophys. Res.*, *79*, 966–971, doi:10.1029/JA079i007p00966.

Stone, E. C., A. M. Frandsen, R. A. Mewaldt, E. R. Christian, D. Margolies, J. F. Ormes, and F. Snow (1998), The advanced composition explorer, *Space Sci. Rev.*, *86*, 1–22, doi:10.1023/A:1005082526237.

Thaller, S. A., et al. (2015), Van Allen Probes investigation of the large-scale duskward electric field and its role in ring current formation and plasmasphere erosion in the 1 June 2013 storm, *J. Geophys. Res. Space Physics*, *120*, 4531–4543, doi:10.1002/2014JA020875.

Valek, P. W., J. Goldstein, J.-M. Jahn, D. J. McComas, and H. E. Spence (2015), First joint in situ and global observations of the medium-energy oxygen and hydrogen in the inner magnetosphere, *J. Geophys. Res. Space Physics*, *120*, 7615–7628, doi:10.1002/2015JA021151.

Vallat, C., I. Dandouras, P. C. Brandt, and D. G. Mitchell (2004), First comparison between ring current measurements by Cluster/CIS and IMAGE/HENA, *J. Geophys. Res.*, *109*, A04213, doi:10.1029/2003JA010224.

Vallat, C., et al. (2007), Ion multi-nose structures observed by Cluster in the inner magnetosphere, *Ann. Geophys.*, *25*, 171–190, doi:10.5194/angeo-25-171-2007.

Weimer, D. R. (1996), A flexible, IMF dependent model of high latitude electric potentials having "space weather" applications, *Geophys. Res. Lett.*, *23*, 2549–2552.

Wygant, J. R. (2013), Modified GSE (mGSE) coordinates. [Available at: https://www.space.umn.edu/wp-content/ uploads/2013/11/.]

Wygant, J. R., et al. (2013), The electric field and waves instruments on the radiation belt storm probes mission, *Space Sci. Rev.*, *179*, 183–220, doi:10.1007/s11214-013-0013-7.

Zhang, J.-C., et al. (2015), "Trunk-like" heavy ion structures observed by the Van Allen Probes, *J. Geophys. Res. Space Physics*, *120*, 8738–8748, doi:10.1002/2015JA021822.